Endothelin B receptor inhibition rescues aging-dependent neuronal regenerative decline

Rui Feng[1#], Sarah F. Rosen[1#], Irshad Ansari[1], Sebastian John[1], Michael B. Thomsen[2], Oshri Avraham[1$], Cedric G. Geoffroy[3] and Valeria Cavalli[1.4,5*]

[1] Department of Neuroscience, Washington University School of Medicine, St. Louis, MO 63110, USA.

[2] CS27 Bioinformatics, Springboro, OH, USA.

[3] Department of Neuroscience & Experimental Therapeutics, Texas A&M Health Science Center, Bryan, TX, 77807, USA

[4] Center of Regenerative Medicine, Washington University School of Medicine, St. Louis, MO 63110, USA.

[5]Hope Center for Neurological Disorders, Washington University School of Medicine, St. Louis, MO 63110, USA.

*Correspondence to: cavalli@wustl.edu

[#] equal contribution

[$] current address: Department of Cellular Biology, University of Georgia, Athens, GA 30602

Valeria Cavalli, Department of Neuroscience, Washington University School of Medicine,

MSC 8108-96-07, 660 South Euclid Avenue, St. Louis, MO 63110-1093.

Phone: +1(314)362-3540, Fax: +1(314)362-3446.

One Sentence Summary:

Inhibition of endothelin signaling improves nerve regeneration after central and peripheral injuries and counters age-related regenerative decline.

Abstract:

Peripheral sensory neurons regenerate their axons after injury to regain function, but this ability declines with age. The mechanisms behind this decline are not fully understood. While excessive production of endothelin 1 (ET-1), a potent vasoconstrictor, is linked to many diseases that increase with age, the role of ET-1 and its receptors in axon regeneration is unknown. Using single cell RNA sequencing, we show that satellite glial cells (SGCs), which completely envelop the sensory neuron soma residing in the dorsal root ganglia (DRG), express the endothelin B receptor (ETBR), while ET-1 is expressed by endothelial cells. Inhibition of ETBR *ex-vivo* in DRG explant cultures improves axon growth in both adult and aged conditions. *In vivo,* treatment with the FDA-approved compound, Bosentan, improves axon regeneration and reverses the age-dependent decrease in axonal regenerative capacity. Single-nuclei RNA sequencing and electron microscopy analyses reveal a decreased abundance of SGCs in aged mice compared to adult mice. Additionally, the decreased expression of connexin 43 (Cx43) in SGCs in aged mice after nerve injury is partially rescued by Bosentan treatment. These results reveal that inhibiting ETBR function enhances axon regeneration and rescues the age-dependent decrease in axonal regenerative capacity, providing a potential avenue for future therapies.

Keywords:

Dorsal root ganglion (DRG), Endothelin B receptor (ETBR), Connexin 43, Bosentan, Satellite glial cells (SGCs), Axon regeneration, Nerve injury, Aging.

INTRODUCTION

Peripheral nerve injuries, resulting from traumatic injuries, lesions, degenerative diseases, and neuropathies, have a major impact on patient's functioning and quality of life (Maita et al., 2023). While neurons in the peripheral nervous system regenerate their axons after nerve injury, functional recovery remains very limited because of the slow growth rate of axons and the often long distances that growing axons face to reconnect with their initial targets (Hoke, 2006). Unfortunately, the ability of injured neurons to regenerate their axons declines with age (Pestronk et al., 1980; Vaughan, 1992; Verdu et al., 2000), contributing to increases in healthcare costs and the risk of long-term disability (Pestronk et al., 1980; Vaughan, 1992; Verdu et al., 2000; Yun, 2015). Thus, discovery of therapeutics that promote axon regeneration and counter age-related decline in regenerative capacity is vital.

Primary sensory neurons, with their cell soma located in the dorsal root ganglia (DRG), convey sensory information from peripheral tissue to the brain via the spinal cord, and represent a useful model to identify the molecular and cellular mechanisms that promote axon regeneration. After injury, successful axonal regeneration of sensory neurons requires activation of neuronal-intrinsic epigenetic, transcriptional, and translational programs (He and Jin, 2016; Mahar and Cavalli, 2018; Rishal and Fainzilber, 2014; Tedeschi and Bradke, 2017). Additionally, non-neuronal cells at the site of injury and in the DRG play an important role in axon regeneration after injury. Satellite glial cells (SGCs) surrounding the cell soma (Avraham et al., 2020; Avraham et al., 2021; Jager et al., 2020) and Schwann cells surrounding the axon (Jessen and Mirsky, 2016), undergo changes in transcriptional states that support axon regeneration. Macrophages recruited to the nerve (Ydens et al., 2020; Zigmond and Echevarria, 2019), and macrophages proliferating in the DRG (Feng et al., 2023) also contribute to axon regeneration after injury.

During aging, decreases in the efficiency of the axonal transport system (Andrews et al., 2016; Black and Lasek, 1979), mitochondrial function (Sutherland et al., 2021), and epigenetic

45 and transcriptional mechanisms (Li et al., 2010) limit the regenerative capacity of neurons.
46 Increases in pro-inflammatory cytokines and macrophage infiltration into the peripheral nerve
47 (Buttner et al., 2018), as well as an increased numbers of T cells in the DRG, have been shown
48 to contribute to the limited regenerative capacity of neurons in aged mice (Zhou et al., 2022).
49 Additionally, age-related decline in the de-differentiation, activation, and senescence of Schwann
50 cells hampers axonal re-growth in damaged peripheral nerves (Fuentes-Flores et al., 2023; Kang
51 and Lichtman, 2013; Painter et al., 2014). While changes in SGCs morphology (Pannese et al.,
52 1996), as well as changes in SGCs-neuronal coupling have been reported with age (Huang et al.,
53 2006; Procacci et al., 2008), the contribution of SGCs to age-dependent decreases in axonal
54 regenerative capacity has not been investigated.

55 Endothelin B receptor (ETBR), a G-protein coupled receptor, is expressed in SGCs
56 (Mapps et al., 2022; Pomonis et al., 2001). One of the ligands for ETBR, Endothelin- 1 (ET-1), is
57 a potent vasoconstrictor secreted by endothelial cells and is the predominant isoform of
58 endothelin in the human cardiovascular system (Luscher and Barton, 2000; Yanagisawa et al.,
59 1988). Previous studies in trigeminal and nodose ganglia have shown that ET-1 activates SGCs
60 through ETBR and reduces gap junction coupling *in vitro* (Feldman-Goriachnik and Hanani, 2017).
61 Studies in astrocytes, which share many functional and molecular features with SGCs (Avraham
62 et al., 2022; Avraham et al., 2020; Hanani and Verkhratsky, 2021) have shown that ETBR
63 inhibition reduces reactive astrocytes and may be a beneficial target to modulate brain diseases
64 (Koyama, 2021). Additional studies in astrocytes have shown that ET-1 signaling via ETBR
65 inhibits the expression of Connexin 43 (Cx43) and reduces gap junction mediated coupling
66 (Blomstrand et al., 2004; Rozyczka et al., 2005). Cx43 is the most highly expressed member of
67 the connexin family in SGCs (Avraham et al., 2022; Huang et al., 2005) and its expression
68 decreases during aging (Procacci et al., 2008). Notably, ET-1 production increases with age and
69 is linked to many age-associated diseases (Barton, 2014; Jankowich and Choudhary, 2020;

70 Stauffer et al., 2008). However, the function of ETBR in SGCs is not known, and whether
71 endothelin signaling contributes to axon regeneration and age-dependent axon regenerative
72 decline has not been examined.

73 First, to determine the role of endothelin signaling in axon regeneration, we performed
74 unbiased single-cell RNA-sequencing of lumbar DRG from mice 3 months of age (adult).
75 Examination of endothelins and their receptors showed enrichment of *Edn1,* the gene encoding
76 ET-1 in endothelial cells and *Ednrb*, the gene encoding ETBR*,* in SGCs. Inhibition of ETBR using
77 the selective antagonist BQ788 in DRG explant cultures enhanced axonal outgrowth in adults and
78 restored axonal regenerative capacity in aged conditions. Treatment of adult and aged mice with
79 Bosentan, an FDA-approved ETBR/ETAR antagonist (Clozel et al., 1994), improved axon
80 regeneration after peripheral nerve injury. To further examine the changes in SGCs induced by
81 aging, we performed single-nuclei RNA-sequencing (snRNA-seq) and transmission electron
82 microscopy of DRG cells from adult and 21-month-old mice (aged). We observed decreased
83 abundance of SGCs in aged conditions, together with extensive transcriptional reprogramming in
84 SGCs, reflecting heightened demands for structural integrity, cell junction remodeling, and glia–
85 neuron interactions within the aged DRG microenvironment. Mechanistically, we found that
86 Bosentan treatment increased expression of Cx43 in SGCs after injury in adult and age mice.
87 These results suggest that ETBR signaling limits axon regeneration after nerve injury and plays
88 a role in age-related decline in regenerative capacity. Thus, ETBR antagonism may be a potential
89 therapeutic avenue to enhance axon growth after nerve injury and to restore axon regenerative
90 capacity that declines with age.

91

92

RESULTS

Ednrb is highly expressed in SGCs.

The dense vascularization of the DRG cell body area coupled with the high permeability of these capillaries in rodents and human (Godel et al., 2016; Jimenez-Andrade et al., 2008) suggests that neurons and their surrounding SGCs may be influenced by vascular-derived signals. Whole mount preparation of DRG from Lycopersicon Esculentum Lectin (LEL) injected *Fabp7*^{CreER}::Ai14 mouse, which labels SGCs with tdTomato (Avraham et al., 2020) revealed the dense vascularization in the neuronal soma rich area of the DRG, as previously reported (Jimenez-Andrade et al., 2008) (Fig.1A, Figure 1 - Movie S1). Additionally, immunofluorescence staining of neurons and SGCs in the DRG from LEL injected adult mouse demonstrated that blood vessels are closely juxtaposed to SGCs surrounding sensory neuron somas (Fig.1B).

To understand the role of endothelin intercellular signaling on axon regeneration, we first performed single cell RNA sequencing (scRNA-seq) on lumbar DRGs from adult female mice (3 months of age) using the Chromium Single Cell Gene Expression Solution (10 X Genomics), as described previously (Avraham et al., 2022; Avraham et al., 2020; Avraham et al., 2021). We sequenced a total of 16,764 cells from two female biological replicates with an average of 3,579 genes and 12,090 transcripts detected per cell (Figure 1C, Figure 1- Figure supplement 1A-B, see methods for filtering criteria). Following unsupervised clustering, we identified eight clusters corresponding to the principal cell types of the mouse DRG. Examination of the cluster-specific marker genes verified the presence of major cellular subtypes including SGCs (*Fabp7/Kcnj10*), myelinating Schwann cells (*Ncmap/Mag*), non-myelinating Schwann cells (*Scn7a/L1cam*), neurons (*Isl1/Prph*), endothelial cells (*Pecam1/Flt1*), fibroblasts (*Col1a1/Pdgfra*), mural cells (*Rgs5/Notch3*), and macrophages (*C1qa/Aif1*) (Fig.1D, Figure 1- Figure supplement 1C, Figure 1- supplementary Data File 1). We then examined the expression of endothelin and their receptors. Endothelin (*Edn1*) and endothelin-3 (*Edn3)* were expressed in endothelial cells and fibroblasts,

118 respectively (Fig.1 D,G,H). *Ednrb* was enriched in SGCs (Fig.1 D,F), whereas *Ednra* was
119 expressed mainly in Mural cells (Fig.1 D,E). *Ednrb* enrichment in SGCs is consistent with prior
120 studies (Mapps et al., 2022; Pomonis et al., 2001; Tasdemir-Yilmaz et al., 2021). Using a
121 published scRNAseq data set across species (Bhuiyan et al., 2024), we observed similar
122 enrichment of *Ednrb* expression in SGCs in humans (Figure 1- Figure supplement 1D). *Ednrb*
123 mRNA in mouse SGCs was validated by RNA *in situ* hybridization, which showed *Ednrb* co-
124 localized with the SGC marker *Fabp7* (Avraham et al., 2020) (Fig.1I).

125 **Endothelin B receptor inhibition increases axonal growth *in vitro* and *ex vivo.***

126 To investigate the role of ETBR signaling in axonal growth, we used different compounds
127 to inihibit or activate endothelin receptors in dissociated L4-L5 DRG mixed cultures. In these DRG
128 cultures, SGCs lose their adhesive contacts with neuronal soma and adhere to the coverslip as
129 time progresses (Belzer et al., 2010; Valtcheva et al., 2016). Within 24 hours in culture, most
130 SGCs are found close to neurons and display flat morphology (Fig. 2B) (Belzer et al., 2010). In
131 these *in vitro* conditions, ET-1 or ET-3 may be released by endothelial cells or fibroblasts. DRG
132 cells were plated and treated with an ETBR antagonist (BQ788), ETBR agonist (IRL1620),
133 endothelin A receptor (ETAR) antagonist (BQ123), or vehicle for 24 hours (Fig 2A). Neurons were
134 then labeled with antibodies against beta III tubulin (TUJ1) and axonal radial length was quantified.
135 Antagonism of ETBR with BQ788 significantly increased axonal radial length compared to vehicle
136 (Fig.C,D). However, agonism of ETBR with IRL1620 or antagonism of ETAR with BQ123 had no
137 significant effects on axonal radial length compared to vehicle treatment (Fig. 2C,D). These
138 results indicate that ETBR signaling limits axonal growth in *in vitro* mixed culture conditions.
139 Inhibition of ETBR may alter trophic factors produced by SGCs into the culture media, leading to
140 axon growth promoting conditions.

141 To further examine the role of ETBR antagonism on axonal growth, we used DRG explants
142 in which L3-L5 DRGs from adult mice were seeded in matrigel and cultured for 7 days (Feng et

143 al., 2023). Explants were then treated with vehicle or BQ788 at days in vitro (DIV) 1 and radial
144 axon growth was assessed at DIV7 by measuring the length of 50 or more axons per explant (Fig
145 2E). Radial axon growth was significantly increased in explants treated with BQ788 compared to
146 vehicle treatment (Fig. 2F-G). To confirm that the *in vivo* morphology of SGCs enveloping
147 neuronal somas was preserved, DRG explants were immunostained with TUJ1 for neurons and
148 FABP7 for SGCs at DIV 7 (Fig. 2H). These results further indicate that ETBR signaling limits
149 axon growth capacity in an *ex-vivo* model.

150 **Bosentan treatment improves axon regeneration after nerve injury.**

151 To determine the potential role of ETBR in regulating nerve regeneration *in vivo*, we used
152 our established *in vivo* regeneration assays (Avraham et al., 2020; Cho and Cavalli, 2012; Cho et
153 al., 2015; Cho et al., 2013) in combination with the FDA-approved compounds that antagonize
154 endothelin receptors, Bosentan and Ambrisentan. These compounds have been utilized to treat
155 pulmonary arterial hypertension, and their safety and efficacy have been demonstrated through
156 various clinical trials (Chen et al., 2018; Galie et al., 2008; Peacock et al., 2015; Rubin et al.,
157 2002). Bosentan is an antagonist of both ETAR and ETBR (Clozel et al., 1994), while Ambrisentan
158 is an antagonist selective for ETAR (Humbert et al., 2004; Newman et al., 2007). Adult mice were
159 treated orally with vehicle, Bosentan or Ambrisentan 2 hours prior to receiving a sciatic nerve
160 crush (SNC) injury. Axon regeneration was assessed 24 hours after injury by measuring the
161 intensity of SCG10 labeled axons, a marker for regenerating axons (Shin et al., 2014) (Fig.3A-E).
162 Since axon growth is relatively slow 24 hours post injury (Shin et al., 2012), we first determined
163 whether ETBR inhibition could accelerate axon growth in the first 24 hours. (Shin et al., 2012;
164 Smith and Skene, 1997). SCG10 intensity was measured distal to the crush site, which was
165 determined according to the highest SCG10 intensity along the nerve (Avraham et al., 2020; Cho
166 et al., 2013; Feng et al., 2023; Shin et al., 2014) and axon elongation was quantified by
167 measurement of the 10 longest axons, as previously described (Carlin et al., 2019) (Fig.3B). A

168 50% regeneration index was quantified by normalizing the average SCG10 intensity at distances
169 away from the crush site to the SCG10 intensity at the crush site, to account for both the length
170 and number of regenerating axons past the crush site and plotting the distance at which SCG10
171 intensity is half of that at the crush site (Cho et al., 2013; Feng et al., 2023) (Fig.3C). Mice that
172 received Bosentan had significantly longer axons and a higher 50% regeneration index 1 day
173 after SNC compared to mice that received vehicle, whereas mice that received Ambrisentan had
174 no significant differences in axon regeneration compared to vehicle (Fig.3B-D). Quantification of
175 the percentage of SCG10 intensity normalized to the crush site at several distances from the
176 injury was also greater in Bosentan treated mice compared to vehicle (Fig.3E). Similarly, at 3 days
177 post SNC, mice that received Bosentan 2 hours before SNC, and then every 24 hours, had
178 improved axon regeneration compared to vehicle, whereas mice that received Ambrisentan had
179 no significant differences in axon regeneration compared to vehicle (Figure 3 - Figure supplement
180 1A-E). Examination of *Edn1, Ednra, and Ednrb* mRNA by RT-qPCR and ETBR by western blot in
181 non-treated mice showed no significant differences in mRNA or protein levels at 3 days post SNC
182 compared to control (Figure 3 - Figure supplement 1F-H). These results suggest that, although
183 ETBR levels do not change after injury, ETBR antagonism increases axon regeneration after
184 peripheral nerve injury at both 1 and 3 days. We next sought to determine whether Bosentan
185 treatment over the course of nerve regeneration improves target re-innervation. Regenerating
186 axons of sciatic nerves extend to the epidermis and start to re-innervate the skin of the hind paw
187 at ~2–3 weeks after injury. We administered Bosentan or vehicle 2 hours prior to SNC, then daily
188 for 7 days, followed by once a week for 2 weeks (Fig. 3F). Intraepidermal nerve fiber density
189 (IENFD) in glabrous skin of the hind paw was assessed by quantification of PGP9.5 positive nerve
190 fibers per millimeter of skin 24 days after SNC. Mice that received Bosentan had a trend towards
191 increased IENFD compared to vehicle-treated mice (Fig.3 G,H). These results suggest that
192 Bosentan treatment may accelerate target re-innervation after injury.

193 We next tested if inhibition of ETBR influences the conditioning injury paradigm, in which
194 a prior nerve injury increases the growth capacity of neurons (Smith and Skene, 1997). DRG
195 neurons from mice that received Bosentan or Ambrisentan 2 hours before SNC, and then every
196 24 hours for three days, were cultured and axon growth capacity was quantified by measuring the
197 axon radial length and TUJ1 positive area (Fig.3J-M). In uninjured condition, neurons extend short
198 neurites, whereas a prior nerve injury leads to neurons growing longer neurites (Fig. 3J-M), as
199 expected (Smith and Skene, 1997). Bosentan, but not Ambrisentan, enhanced the axon radial
200 length of DRG neurons cultured from uninjured adult mice, partially mimicking the conditioning
201 injury, and also increased the growth capacity of injured neurons (Fig.3J-M). Since the selective
202 ETAR antagonists, BQ123 and Ambrisentan, had no significant effects on axon regeneration after
203 nerve injury (Fig. 2A-C, 3A-E), our results indicate that ETBR signaling limits axon regenerative
204 capacity.

205 To determine the effects of Bosentan treatment on axon regeneration in a model with
206 lower regenerative capacity, axon growth after dorsal root crush (DRC) injury was assessed
207 (Figure 3 - Figure supplement 2A). Following DRC injury, axon growth occurs at about half the
208 rate of peripheral axons (Oblinger and Lasek, 1984; Wujek and Lasek, 1983) and our previous
209 work has shown that manipulation of SGCs after DRC improves axon regeneration (Avraham et
210 al., 2021). Axon regeneration at 3 days post DRC was assessed by measuring SCG10 intensity,
211 as described above. Mice that received Bosentan had significantly more axon regeneration along
212 the dorsal root compared to vehicle (Figure 3 - Figure supplement 2B-E). Together, these results
213 indicate that ETBR inhibition improves axon regeneration after both peripheral and central axon
214 injury in DRG neurons.

215 **Inhibiting ETBR rescues aging-dependent axonal regenerative decline.**

216 It is known that elevated tissue or plasma concentrations of ET-1 occurs with age
217 (Jankowich and Choudhary, 2020). We thus evaluated the expression levels of ET-1 and ETBR

218 in DRG of adult and aged mice by western blot. For loading controls, we used both ponceau
219 staining for total protein and GAPDH, as we observed lower levels of GAPDH in aged mice.
220 Regardless of the normalization method, we found that ET-1 levels were significantly elevated in
221 aged mice compared to adult (Figure 4 - Figure supplement 1A). ETBR levels were only elevated
222 in aged mice when normalized to the GAPDH control (Figure 4 - Figure supplement 1BB). These
223 results confirm that ET-1 levels are elevated in DRG tissue in aged mice.

224 To determine the role of ETBR signaling on axon growth during aging, DRG explants from
225 aged (21-month-old) mice were treated with BQ788 or vehicle (Fig.4A). Aged DRG explants
226 treated with BQ788 had significantly increased radial axon length compared to vehicle (Fig.4B-
227 C). In fact, aged explants treated with BQ788 had significantly more radial axon growth than to
228 that of adult (3-month old) vehicle explants (Fig 4C). *In-vivo* Bosentan pre-treatment in aged mice
229 also increased radial axon growth in DRG explants (Figure 4 - Figure supplement 1C-E). Axon
230 regeneration after peripheral nerve injury in aged mice *in vivo* was assessed by measuring
231 SCG10 intensity in adult and aged mice 3 days post SNC. As expected, aged vehicle-treated
232 mice had significantly less axon regeneration compared to adult vehicle-treated mice (Fig. 4D-G)
233 (Zhou et al., 2022). However, aged mice treated with Bosentan had significantly increased axon
234 regeneration compared to vehicle-treated aged mice. Indeed, treatment with Bosentan increased
235 axon regeneration in aged mice to levels similar to vehicle-treated adult mice (Fig.4D-G). These
236 results indicate that inhibition of ETBR rescues the age-dependent decline in axon regeneration.

237 **Aging affects SGCs abundance, transcriptional profile, and morphology.**

238 To examine the effect of age on the transcriptional profiles of SGCs, we isolated lumbar
239 DRG from adult and aged mice and performed single nucleus RNA-seq using the Illumina Single
240 Cell 3' RNA Prep (Illumina). We chose this microfluidics-free system for single-nuclei mRNA
241 capture, barcoding, and library prep because it has been shown to be gentler and capture rarer
242 cell populations in the brain (Frazel et al., 2023), and our initial attempt with 10X Genomics on

243 aged tissue yielded insufficient amount of viable cells. After quality control and filtering, we
244 recovered 17,852 high-quality single-nucleus transcriptomes (10,717 adult, 7,135 aged) across
245 three biological replicates (one adult, two aged), with an average of 2,854 genes and 9,899
246 transcripts detected per cell (Figure 5 - Figure supplement 1A-B). Following RPCA-based
247 integration by age, unsupervised clustering identified 16 distinct cell types (Fig. 5A). These
248 included four principal neuronal classes (PEP, NF, NP, TH), three glial cell types (SGCs, NMSC,
249 MSC), three previously described fibroblast subsets (EF, EM, PM) (Zhao et al., 2022) vascular
250 endothelial cells, mural cells, and several immune-related populations (MYEL, TC, BC, HSC) (Fig.
251 5A). Each cluster was distinguished by multiple unique marker genes, consistent with prior DRG
252 single-cell studies (Avraham et al., 2020; Avraham et al., 2021; Jung et al., 2023; Mapps et al.,
253 2022; Renthal et al., 2020; Usoskin et al., 2015) (Fig. 5B).

254 To further investigate aging-associated transcriptional changes in SGCs, we performed
255 differential expression analyses followed by GO (gene ontology) and KEGG (Kyoto Encyclopedia
256 of Genes and Genomes) pathway enrichment (Figure 5 - Figure supplement 1C,D). Many genes
257 were upregulated in aged SGCs, including those involved in cell junction assembly, adherens and
258 tight junction pathways, and focal adhesion, indicating significant alterations in cell-cell contacts.
259 In addition, we observed changes in pathways regulating cell projection organization, synapse
260 organization and structure, and supramolecular fiber organization, suggesting widespread
261 remodeling of SGC architecture. Several signaling pathways implicated in structural and
262 morphogenetic processes, such as axon guidance and Wnt signaling, were also enriched in aged
263 SGCs. Genes related to cellular senescence were also upregulated in aged SGCs (Figure 5 -
264 Figure supplement 1D). Collectively, these results suggest that aging triggers extensive
265 transcriptional reprogramming in SGCs, reflecting heightened demands for structural integrity,
266 cell junction remodeling, and glia–neuron interactions within the aged DRG microenvironment.

267 Comparative analysis of relative cell-type abundances between adult and aged DRG
268 revealed a marked decrease in SGC representation and a corresponding rise in immune cell and
269 neuronal populations in aged samples (Fig. 5C-E). Changes in morphology of SGCs have been
270 reported with age in rabbit, with a decrease in SGCs number and SGCs retracting and leaving
271 the neuronal soma exposed to the extra cellular DRG environment (Pannese et al., 1997;
272 Pannese et al., 1996). In the DRG of aged mice, neurons appeared to be enveloped by SGCs
273 similarly to adults (Huang et al., 2006), but quantification of SGCs number were not performed.
274 We thus examined the impact of age on SGCs morphology and number by transmission electron
275 microscopy (TEM). In adult mice, each sensory neuron was enveloped by its own SGCs sheath
276 as described previously (Pannese, 1981; Pannese, 2010). In aged mice however, SGCs
277 appeared thinner compared to adult mice (Fig 5F). Quantification of the average width of SGCs
278 per neuron demonstrated a significant decrease during aging (Fig.5G). Quantification of the
279 number of SGC nuclei per neuronal soma in TEM images revealed that 21-month-old mice had
280 fewer SGCs per neuron compared to 2-month-old mice (Fig.5H), indicating a decrease in SGC
281 number with age. These results suggest that, in addition to significant transcriptional changes,
282 SGCs may undergo atrophy during aging.

283 **ETBR inhibition increases the expression of Cx43 in SGCs in adult and aged mice**

284 Cx43 is a member of the connexin family and can form hemichannels and gap junction
285 channels (Mazaud et al., 2021). Several studies suggest that both Cx43 gap junctions and
286 hemichannels operate in SGCs and have an important role in communication between SGCs and
287 between SGCs and sensory neurons (Hanani and Spray, 2020; Retamal et al., 2017). Cx43 in
288 human SGCs was proposed to play a key role in the protection and maintenance of neurons in
289 spiral ganglia (Liu et al., 2014). Past studies in mice have shown that Cx43 expression in SGCs
290 decreases during aging (Procacci et al., 2008). In cultured SGCs and astrocytes, endothelin
291 signaling reduces the expression of Cx43 (Blomstrand et al., 2004; Feldman-Goriachnik and

292 Hanani, 2017; Rozyczka et al., 2005). We thus investigated the role of endothelin signaling and
293 aging in Cx43 expression in SGCs. *Gja1*, the gene for Cx43, is enriched in SGCs in both adult
294 and aged mice (Fig.6A), as expected (Procacci et al., 2008). Changes in *Gja1* expression level
295 with age were statistically difficult to assess because there were less SGCs in aged mice
296 compared to adult, and *Gja1* is only detected in 20% of SGCs. We therefore quantified Cx43
297 protein expression level in SGCs by immunofluorescence (Figure 6 - Movie S2). The level of Cx43
298 expression, measured by both the Cx43 expression area and the number of Cx43 puncta in Fabp7
299 positive SGCs surrounding neuronal soma, was significantly lower in aged mice compared to
300 adult mice (Fig.6C-D), consistent with prior studies (Ohara et al., 2008; Procacci et al., 2008).
301 Nerve injury increased Cx43 levels in both adult and aged vehicle-treated mice and Bosentan
302 treatment led to an increase in Cx43 expression in both adult and aged mice (Fig.6C-E).
303 Examination of Cx43 expression in SGCs after DRC in adult mice showed no increase in Cx43
304 levels compared to uninjured mice, but Bosentan-treated mice increased Cx43 levels compared
305 to vehicle (Figure 6 - Figure supplement 1A-C). These results reveal a correlation between Cx43
306 levels in SGCs and axon regenerative capacity, providing a potential mechanism by which ETBR
307 inhibition with Bosentan may promote axon regeneration after injury (Fig. 6F). Future experiments
308 will determine if Cx43 acts downstream of ETBR and how Cx43 regulates axon regeneration.
309

310 **DISCUSSION**

311 Peripheral nerve injuries have a major impact on patient's functioning and quality of life
312 (Maita et al., 2023). The ability of injured neurons to regenerate their axons declines with age
313 (Geoffroy et al., 2016; Geoffroy et al., 2017; Pestronk et al., 1980; Vaughan, 1992; Verdu et al.,
314 2000), contributing to an increased risk of long-term disability (Pestronk et al., 1980; Vaughan,
315 1992; Verdu et al., 2000; Yun, 2015). Our study shows that ETBR functions in part to limit axonal
316 regenerative capacity and that Bosentan, an FDA-approved ETBR/ETAR antagonist, increases

317 axonal regeneration after peripheral and central axon nerve injury. Furthermore, Bosentan
318 rescues the age-dependent decrease in axonal regenerative capacity. These results suggest that
319 ETBR inhibition may be a beneficial therapeutic to promote axon regeneration after injury.

320 Our results demonstrate that *Ednrb* is highly enriched in SGCs in the DRG, and selective
321 antagonism of ETBR in DRG mixed cultures and DRG explants increases axon outgrowth.
322 Furthermore, we show that Bosentan treatment *in vivo* increases axon growth 1 and 3 days after
323 nerve injury, and long-term Bosentan treatment may improve target reinnervation 3 weeks after
324 injury. It is important to note that in the DRG mixed cultures, SGCs, while still present, do not
325 envelop the neuronal soma as they do in the explant culture and *in vivo.* However, antagonism of
326 ETBR in DRG mixed cultures still increases axon growth. Thus, it is possible that inhibition of
327 ETBR alters the release of trophic factors from SGCs, stimulating the growth potential of neurons
328 and accelerating axon growth. Future studies will be required to unravel how ETBR signaling
329 influences the SGC secretome and its influence on axon growth. Additionally, orchestration of
330 axon regeneration in the nerve depends on multiple cell types. Polarized vascularization in the
331 nerve precedes Schwann cell migration (Bhat et al., 2024; Cattin et al., 2015). Since ETBR is
332 expressed in Schwann cells and has been shown to play a role in Schwann cell generation
333 (Brennan et al., 2000), we cannot rule out the possibility that Bosentan treatment *in vivo* may
334 affect axon regeneration through ETBR in Schwann cells in addition to SGCs. However, given
335 our results demonstrating that DRG explants maintain the SGC-sensory neuron morphology, and
336 axon outgrowth in this model does not rely on repair Schwann cells, we can conclude that blocking
337 ETBR signaling in SGCs contributes to increasing axon outgrowth, at least in the initial axon
338 growth phase. Together, these results suggest a novel molecular mechanism in peripheral nerve
339 regeneration.

340 We hypothesize that the major ligand acting on ETBR in the DRG is ET-1. This is based
341 on our scRNA-seq data in the DRG showing *Edn1/*ET-1 enrichment in endothelial cells, as well

342 as the dense vascularization in DRG. Additionally, the observation that elevated tissue or plasma
343 concentrations of ET-1 occurs with age (Jankowich and Choudhary, 2020) and our results
344 showing that ET-1 levels increase in the aged DRG support the notion that ETBR signaling in
345 SGCs limits axon regenerative capacity in aged mice. However, other studies have suggested
346 that ET-1 is also expressed by small diameter neurons in human DRG (Giaid et al., 1989), thus it
347 is possible that neuronally derived ET-1 may act on ETBR in SGCs. Additionally, our scRNA-seq
348 data shows that another ligand for ETBR, *Edn3*/ET-3, is enriched in fibroblasts in the DRG. While
349 ET-1 binds to ETAR and ETBR with the same affinity, ET-3 shows a higher affinity to ETBR than
350 to ETAR (Davenport et al., 2016). It also has been shown in cultured cortical astrocytes that
351 application of either ET-1 or ET-3 leads to a robust inhibition of connexin Cx43 expression
352 (Rozyczka et al., 2005). Thus, we cannot exclude the possibility that ET-3 may act on ETBR in
353 SGCs to regulate axon growth. Lastly, as our scRNA-seq data shows that *Ednra* is enriched in
354 mural cells (Chen et al., 2000), it is also possible that endothelin's impact on vascular permeability
355 through ETAR activity contributes to axon regeneration. Future experiments will be required to
356 test how injury and age affects vascular permeability in the DRG. Nonetheless, whether via ET-1
357 or ET-3, our results highlight that ETBR acts to limit spontaneous sensory axon regeneration, and
358 that inhibition of ETBR promotes axon regeneration.

359 Although a biologically intrinsic mechanism to inhibit axon regeneration appears
360 counterintuitive, other mechanisms limiting axon regenerative capacity have been reported.
361 Axonally synthesized proteins typically support nerve regeneration through retrograde signaling
362 and local growth mechanisms (Sahoo et al., 2018). RNA binding proteins (RBP) are needed for
363 this process and other aspects of post-transcriptional regulation of neuronal mRNAs. One such
364 RBP, the RNA binding protein KHSRP is locally translated following nerve injury, promotes decay
365 of other axonal mRNAs and slows axon regeneration (Patel et al., 2022). Additionally, Rho
366 signaling pathway is an inhibitory regulatory mechanism that slows the growth of spiral ganglion

367 neurite in culture (Lie et al., 2010). These mechanisms may function to limit plasticity and prevent
368 maladaptive neural rewiring that can happen after injury (Costigan et al., 2009), but can also
369 hinder beneficial recovery after injury. Whether ETBR inhibition over a longer time period has
370 consequences on target innervation and functional recovery will require further investigation.

371 Investigation of the effects of aging on sensory ganglia have shown that the number of
372 neurons decrease with age in different species including human, cats and rats (Aldskogius and
373 Risling, 1989; Nagashima and Oota, 1974; Schmalbruch, 1987). The effect of age on SGCs has
374 received less attention, but we know that the number of SGCs decrease with age in the rabbit
375 (Pannese et al., 1997; Pannese et al., 1996). In agreement with these prior studies, our snRNA-
376 seq and morphology data reveal a marked decrease in SGC representation in the DRG of aged
377 mice. Our EM data indicate that the number of SGCs surrounding each neuronal soma decreases
378 with age and appear thinner, suggesting SGC atrophy in addition to SGC loss. KEGG pathway
379 analysis also suggests that aged SGCs transition into a senescent phenotype during aging, a
380 state where cells no longer divide but remain viable. SGCs have the capacity to divide, although
381 this process is very slow (Maniglier et al., 2022). It was proposed that SGC self-renewal
382 maintained the SGC population through adulthood, ensuring neuronal survival throughout life
383 (Maniglier et al., 2022). This balance may become dysfunctional with age, leading to the
384 accumulation of senescent SGCs. In the nerve, senescence of Schwann cells in aged mice was
385 shown to undermine axonal regeneration, and systemic elimination of senescent cells with
386 senolytic drugs improves axonal regeneration (Fuentes-Flores et al., 2023), raising the interesting
387 possibility that senescent SGCs also contribute to limit axon regeneration in aged mice. Future
388 studies are needed to determine if aged SGCs, similarly to aged Schwann cells, secrete inhibitory
389 factors that limit axon regeneration. We also observed changes in pathways regulating cell
390 projection organization, synapse organization and structure, and supramolecular fiber
391 organization, suggesting widespread remodeling of SGC architecture. Several signaling

392 pathways implicated in structural and morphogenetic processes, such as axon guidance and Wnt
393 signaling, were also enriched in aged SGCs. Collectively, these results suggest that aging triggers
394 extensive transcriptional reprogramming in SGCs, reflecting heightened demands for structural
395 integrity, cell junction remodeling, and glia–neuron interactions within the aged DRG
396 microenvironment.

397 Cx43 is a transmembrane protein that performs canonical gap junction functions, such as
398 connecting adjacent cells and allowing the diffusion of ions and small molecules. Cx43 can also
399 form hemichannels that may have an important role in communication between SGCs and
400 sensory neurons (Retamal et al., 2017). Emerging evidence suggests that connexins can perform
401 non-channel functions, such as protein interaction, cell adhesion, and intracellular signaling
402 (Mazaud et al., 2021). Using our snRNA-seq data to compare *Gja1* levels in adult vs aged SGCs
403 was statistically difficult to interpret, as there were significantly fewer SGCs in aged mice. The
404 histology examining Cx43 protein levels was normalized to total SGCs, and showed a significant
405 decrease in Cx43 puncta/SGC in aged mice, consistent with previous studies and the hypothesis
406 that a prominent decrease in Cx43 is a marker of senescence (Procacci et al., 2008). It has also
407 been shown in SGCs of aged mice that that there is an increase in gap junctions and dye coupling
408 (Huang et al., 2006). This apparent discrepancy could be explained by expression changes in
409 connexin types other than Cx43 that may contribute to the gap junctions. Indeed, our snRNA-seq
410 data revealed changes in other connexins with age, but the percentage of cells expressing these
411 genes and the level of expression was not robust enough to draw meaningful conclusions. Deeper
412 sequencing would likely be required to verify this hypothesis. It is also important to note that, while
413 sequencing is a strong tool, aging has profound effects on post-translational regulation, such as
414 altered protein half-life, defects in protein trafficking, and increased protein degradation (Santos
415 and Lindner, 2017; Skariah and Todd, 2021). Thus, in conjunction with sequencing, examination
416 of protein levels of various connexins in SGCs will be necessary.

417 Our results show that Cx43 in SGCs from both adult and aged injured mice increased with
418 Bosentan treatment compared to vehicle treatment. Studies in cultured SGCs and astrocytes
419 have demonstrated that endothelin signaling reduces gap junctions coupling (Blomstrand et al.,
420 2004; Feldman-Goriachnik and Hanani, 2017; Rozyczka et al., 2005). Thus, we hypothesize that
421 ETBR inhibition in SGCs contributes to axonal regeneration by increasing Cx43 levels, gap
422 junction coupling or hemichannels, facilitating SGC-neuron communication. However, it is also
423 possible that other mechanisms downstream of ETBR signaling in SGCs contribute to axon
424 regeneration. For example, glutamate uptake by SGCs is regulated by glutamate transporters
425 GLT-1 and GLAST and is crucial for neuronal function (Berger and Hediger, 2000; Hanani and
426 Verkhratsky, 2021; Ohara et al., 2008). Studies in astrocytes suggest that endothelin exposure
427 reduces glutamate uptake by decreasing transporter expression. One of the functions of GLAST
428 in astrocyte is related to lesion-induced plasticity in the developing brain (Takasaki et al., 2008),
429 suggesting that ETBR might limit axon regeneration by influencing SGCs' glutamate reuptake. As
430 ETBR is a G protein-coupled receptor which interacts with Gi and Gq (but not Gs) (Ham et al.,
431 2024; Tani et al., 2024) its inhibition could have numerous effects on intracellular signaling
432 pathways and transcriptional response in SGCs. Further studies are needed to determine the
433 detailed molecular mechanisms by which ETBR signaling in SGCs limits axon regeneration.

434 Taken together, our results suggest that ETBR signaling limits axon regeneration after
435 nerve injury and contributes to age-related decreases in neuronal regenerative capacity.
436 Bosentan, an FDA approved ETBR/ETAR antagonist, significantly increased axon regeneration
437 in both adult and aged mice, suggesting a potential therapeutic avenue that may be used to
438 enhance axonal regeneration after nerve injury.

439

440

441 **MATERIALS AND METHODS**

442 **Study design**

443 The main goals of this study were to investigate the role of ETBR in axonal regeneration,
444 explore its impact on SGCs in the DRG, and evaluate the therapeutic potential of Bosentan, an
445 FDA-approved drug, on axon regeneration and age-related decline capacity for nerve repair. We
446 performed scRNA-seq and snRNAseq analysis on DRG samples from adult and aged mice. We
447 analyzed samples from mice subjected to various treatments and performed *in vitro* assays
448 including immunofluorescence (IF), Western blotting, quantitative real-time polymerase chain
449 reaction (qPCR), RNA *in situ* hybridization (RNAscope) and TEM. For *in vitro* cell assays, data
450 were collected from at least three independent cultures, as indicated in figure legends. *In vivo* and
451 ex-vivo experiments were conducted using biological replicates, as denoted by the 'n' values in
452 the figure legends. The sample sizes were determined based on previous experience for each
453 experiment, and mice were randomly assigned to the experimental groups whenever possible.
454 No mice, outliers, or other data points were excluded. Details on animal assignment,
455 randomization, and blinding in different experiments are found in the corresponding sections
456 describing each experiment in Materials and Methods.

457 **Animals**

458 Mice of different age groups were included in the study, specifically 2-3-month-old (adult,
459 female and male), 12-month-old (mid-age, female), and 21-month-old (aged, female). Wild-type
460 C57BL/6 mice were purchased from Envigo (Envigo #027) and Jackson Laboratory (Stock No:
461 000664). Ai14 (B6.Cg-Gt(ROSA)26Sortm14(CAG-tdTomato)Hze/J, JAX Stock No: 007914) mice
462 was obtained from The Jackson Laboratory (Madisen et al., 2010). The *Blbp*^{CreER} (*Fabp7*^{CreER})
463 mouse line was a generous gift from Dr. Toshihiko Hosoya (Maruoka et al., 2011). Ai14 mice were
464 crossed with *Fabp7*^{CreER} mice to obtain *Fabp7*^{CreER}::Ai14 mice. Mice were housed in the animal
465 facility at Washington University in St. Louis, where temperature (64-79°F) and humidity (30%-

466 70%) were carefully controlled. They were socially housed in individually ventilated cages, with
467 1-5 mice per cage, and subjected to a 12-hour light/dark cycle (6 am/6 pm). Mice had unrestricted
468 access to food and water throughout the study. All experimental procedures were conducted
469 following the approved protocol (21-0104) by the Institutional Animal Care and Use Committees
470 of Washington University in St. Louis. All experiments adhered to relevant guidelines and
471 regulations. The study obtained approval from the Washington University School of Medicine
472 Institutional Animal Care and Use Committee (IACUC) under protocol A-3381-01. The mice were
473 housed and cared for in the animal care facility at Washington University School of Medicine,
474 which is accredited by the Association for Assessment & Accreditation of Laboratory Animal Care
475 (AALAC) and complies with the PHS guidelines for Animal Care. The facility has been accredited
476 since 7/18/97, and its USDA Accreditation Registration number is 43-R-008.

477 **Primary adult DRG culture**

478 L4 and L5 DRGs were collected from 12-week-old mice and placed in cold dissection
479 medium composed of HBSS (Thermo Fisher, Gibco; Catalog#: 14175-079) with 10% 1M HEPES
480 (Thermo Fisher, Gibco; Catalog#: 15630080). The DRGs were then transferred to freshly
481 prepared pre-warmed dissociation medium containing 15U/mL Papain suspension (Worthington
482 Biochemical; Catalog#: LS003126), 0.3mg/mL L-cysteine (Sigma; Catalog#: C7352), 0.1mg/mL
483 Deoxyribonuclease I (Worthington Biochemical; Catalog#: LS002139), and 10% 1M HEPES in
484 HBSS. The samples were incubated at 37°C for 20 minutes. After washing the samples twice with
485 pre-warmed HBSS, collagenase (150μg/mL; Sigma; Catalog#: C6885) was added, and the
486 samples were incubated at 37°C for another 20 minutes. Following two additional washes with
487 pre-warmed HBSS, the resulting single-cell suspension was gently triturated and resuspended in
488 complete medium consisting of Neurobasal™-A Medium (Thermo Fisher, Gibco; Catalog#:
489 12349015) supplemented with B-27™ Plus Supplement (Thermo Fisher, Gibco; Catalog#:
490 A3582801) and GlutaMAX™ Supplement (Thermo Fisher, Gibco; Catalog#: 35050061). The cell

491 suspension was then passed through 70-micron cell strainers. The single-cell suspension was
492 then centrifuged at 500 × rpm at 4°C for 5 minutes, and the cell pellet was resuspended in
493 complete Neurobasal medium. Cells were seeded on poly-D-lysine (PDL)-coated 18mm
494 coverslips at a density of 1.0 × 10^3 cells per coverslip. For drug treatment, BQ788 (Sigma;
495 Catalog #B157) 1□M, BQ123 (R&D system; Catalog #: 1188) 1mM, IRL620 (Sigma; Catalog #:
496 SCP0135) 100nM or DMSO as vehicle control were added directly to the complete medium just
497 before suspending the cells and seeding them into separate culture plates and incubated for the
498 entire 24-hour culture period. The animals were randomized into groups and the researcher was
499 not blinded during the analysis.

500 **DRG Explant culture**

501 L3-L5 DRGs from male and female 8-wk- or 21-months- old mice were collectedinto cold
502 explant media [Putrescine Dihydrochloride (Sigma Aldrich, Catalog# p7505), L-Glutamine
503 (Thermofisher, Catalog# A2916801), Insulin Transferrin Selenium (Sigma Aldrich, Catalog#
504 A4034), Glucose (Sigma Aldrich, Catalog# G7021), Basal Medium Eagle (Thermofisher,
505 Catalog# 35050061), Bovine Serum Albumin (Sigma Aldrich, Catalog# A9430), Ham's F-12
506 Nutrient Media (Thermofisher, Catalog# 11765-054)]; DRG roots were trimmed to 2mm with a
507 sharp scalpel, then placed into a 15ul drop of a 1:1 ratio of explant media and ECM Gel from
508 Engelbreth-Holm-Swarm murine sarcoma (Sigma Aldrich, Catalog# E1270) in cell culture plates.
509 24 hours after plating, Nerve Growth Factor (NGF) (Alomone, Catalog# N-240) was added to the
510 media Note that NGF does not promote significant effects on axon growth in DRG explants, but
511 stimulates glial cell migration (Klimovich et al., 2020). We opted to included NGF in our explant
512 assay to increase the potential of stimulating axon regeneration with pharmacological
513 manipulations of ETBR. Seven days after plating, explants were fixed and stained for TUJ1 to
514 quantify axon length.

515

516 **Sciatic nerve and dorsal root injuries**

517 Sciatic nerve crush injuries were performed following established protocols (Avraham et
518 al., 2021). Briefly, 12-week-old mice were anesthetized using 1.5% inhaled isoflurane. A small
519 skin incision was made to expose the sciatic nerve at mid-thigh level, approximately 1.2 cm from
520 the L4 dorsal root ganglion (DRG). The sciatic nerve was fully crushed for 10 seconds using
521 0.1mm forceps (#55). The wound was closed with wound clips, and the mice were placed on a
522 warming pad until fully awake. At the designated time points post-surgery, L4 and L5 dorsal root
523 ganglia were dissected for further analysis. The animals were randomized into groups.

524 Dorsal root crush injuries were performed as previously described (Avraham et al., 2021).
525 Surgery was conducted on 12-week-old mice under 1.5% inhaled isoflurane anesthesia. A small
526 midline skin incision (~1 cm) was made over the thoracic vertebrae at L2-L3, followed by
527 paraspinal muscle release and stabilization of the vertebral column with metal clamps under the
528 L2-L3 transverse processes. Dorsal laminectomy was performed using forceps at the L2-L3 level,
529 and the right L3-L5 dorsal roots were crushed simultaneously for 5 seconds. The proximity
530 between L3-L5 roots resulted in a crush distance of 1-2 mm to L3 DRG, 4-5 mm to L4 DRG, and
531 7-8 mm to L5 DRG. The crushing process exerted force on the roots, causing disruption of nerve
532 fibers without interrupting the endoneurial tube. Paraspinal muscles were sutured using 6-0
533 sutures (Ethicon, Catalog#: J212H), and the wound was closed with clips. Mice were placed on a
534 warming pad until fully awake, and L4 dorsal root ganglia and L4 dorsal roots were dissected at
535 3 days post injury. The animals were randomized into groups.

536 **Drug Administration**

537 To assess the *in vivo* functions of endothelin receptors, pharmacological testing was
538 conducted. For the analysis of nerve regeneration at one day post-injury, oral gavage
539 administration of Ambrisentan (Tocris, Catalog# 5828, 10 mg/kg body weight) (Kappes et al.,
540 2020) and Bosentan (Sigma, Catalog#PHR2708, 10 mg/kg body weight) (Pinho-Ribeiro et al.,

541 2014) was performed 2 hours before the injury, with sample collection taking place 24 hours after
542 the injury. For the analysis of nerve regeneration after 3 days post-injury, Ambrisentan (10 mg/kg
543 body weight) and Bosentan (10 mg/kg body weight) were administered via oral gavage 2 hours
544 before the injury and once daily after the injury. The treatments were randomized within the
545 surgery mice group.

546 **Western Blotting**

547 L4-L5 DRGs were collected and lysed in RIPA Buffer (Cell Signaling, catalog #9806) and
548 heated at 99°C for 10 min. The protein lysates were then loaded onto an 10% Ready Gel® Tris-
549 HCl Precast Gels (BioRad, catalog#1611119) in running Buffer (BioRad, Catlog#1610744) and
550 transferred to 0.2 □m PVDF membranes (BioRad, Catalog#1620216). The membranes were
551 blocked in 5% non-fat dry milk (BioRad, Catalog#1706404XTU) Tris-Buffered Saline (TBS)
552 containing 0.1% Tween-20 at pH 7.6 for 1 h. Following blocking, the membranes were incubated
553 overnight at 4°C with primary antibodies Rabbit-anti-ETBR (Abcam, Catalog# ab117529, 1:500)
554 Mouse-anti-ET-1 1:500 (Invitrogen, Catalog# MA3-005) Rabbit-anti-GAPDH 1:5000 (Cell
555 Signaling, Catalog# 5174s) in blocking buffer. Afterward, the membranes were washed three
556 times with TBST (Tris-buffered saline with 0.1% Tween-20) and then incubated with horseradish
557 peroxidase-conjugated anti-rabbit (Invitrogen, Catalog# 31460,1:5000) or anti-mouse (Invitrogen,
558 Catalog # 31430,1:5000) antibodies in blocking buffer for 1 h at room temperature. Subsequently,
559 the membranes were washed three times with TBST and developed using SuperSignal™ West
560 Dura (Thermo Scientific, Catalog# 34075). The ChemiDoc System (Bio-Rad) was used to image
561 the membranes. For subsequent analysis, the membranes were stripped using a mild stripping
562 buffer composed of (1.5% glycine, 0.1% SDS, and 1% Tween -20, pH2.2 in ddH_2O). Following
563 stripping, the protocol was repeated for GADPH staining (Santa Cruz Biotechnology, Catalog #sc-
564 51907, 1:8000) as the loading control. The resulting images were analyzed using Fiji software.

565 To quantify the protein levels, the intensity of ET-1 or ETBR was normalized to the intensity of
566 GADPH. The researcher was not blinded during the analysis.

567 **Quantitative real time PCR**

568 For qRT-PCR, L4 and L5 DRGs of each mouse were collected and total RNA was
569 extracted using RNeasy Mini Kit (QIAGEN, Cat# 74104). For cDNA synthesis, 500 ng of RNA
570 was converted into cDNA with the High-Capacity cDNA Reverse Transcription Kit (ThermoFisher,
571 Catalog# 4368814) according to manufacturer's specifications. Quantitative PCR was completed
572 using the PowerUp™ SYBR™ Green Master Mix (ThermoFisher, Cat# A25780) using gene-
573 specific primers (resource table) from Primerbank (https://pga.mgh.harvard.edu/primerbank/).
574 qRT-PCR was performed on a QuantStudio 6 Flex System. Expression fold change for each gene
575 of interest was calculated using the ΔCq method and normalized to the expression fold change
576 of *Gadph* expression compared to controls. The researcher was not blinded during the analysis.
577 The detail for each primer was listed in Supplementary Table 1.

578 **Immunohistochemistry**

579 Mice were euthanized with CO_2 asphyxiation and transcardially perfused with PBS
580 followed by 4% paraformaldehyde (PFA). PFA-fixed tissues were incubated in 30% sucrose in
581 phosphate-buffered saline (PBS) overnight at 4 °C, specimens were embedded in optimal cutting
582 temperature compound (OCT) (Tissue-Tek), stored at −80 °C until further processing. Transverse
583 sections of DRG (L4) and longitudinal sections of sciatic nerve were cut on a cryostat at 10μm,
584 and stored at -20 °C until processed. Before staining, sections were warmed to room temperature
585 and dried on a 60 °C slide warmer for 5 mins. Sections were treated with a blocking solution
586 containing 4% normal donkey serum (NDS) (LAMPIRE; Catalog#7332100) with 0.5% Triton X-
587 100 in PBS for 1h at room temperature. Then samples were incubated in the primary antibodies,
588 which were diluted in 1% NDS with 0.3% Triton X-100 in PBS overnight at 4°C. After three PBS
589 rinses, samples were incubated with Alexa Fluor–conjugated secondary antibodies in PBS with

590 0.3% Triton X-100 in 1h, followed by incubation in 300nM 4′,6-diamidino-2-phenylindole (DAPI,
591 Sigma-Aldrich, Catalog# D9542) at room temperature for 10 mins. Samples were rinsed before
592 mounting with ProLong™ Gold Antifade Mountant (Invitrogen, Catalog#:P36930). For co-staining
593 of Cx43 and Fabp7, both of which are rabbit antibodies, the tissue sections were first blocked with
594 10% NDS in PBS containing 0.3% Triton X-100 at room temperature for 1h. Subsequently, the
595 sections were incubated overnight at 4°C with rabbit anti-Cx43 antibody diluted in 0.1% Triton X-
596 100 in PBS. After three rinses with PBS, the samples were incubated with an excess of conjugated
597 Fab Fragment secondary antibody in PBS with 0.3% Triton X-100 for one hour. Following three
598 washes with PBS, the sections were incubated with rabbit anti-Fabp7 antibody, diluted in 0.1%
599 Triton X-100 in PBS, at room temperature for 2h. After three PBS washes, the samples were
600 incubated with Alexa Fluor-conjugated secondary antibodies in PBS with 0.3% Triton X-100 for
601 one hour. Finally, the sections were incubated with DAPI at room temperature for 10 minutes,
602 followed by rinsing and mounting with ProLong™ Gold Antifade Mountant. DRG sections were
603 imaged with a confocal laser-scanning microscope (Zeiss LSM880). Figures showing large
604 longitudinal sciatic nerve sections were produced using EVOS™ M7000 Imaging System with
605 image stitching and/or stack software. For adult DRG culture staining, neurons were fixed in pre-
606 warmed 1%PFA in 7.5% sucrose at 37 °C for 15 mins. Then post-fixed in prewarmed 2%PFA in
607 15% sucrose in 30 mins. Rise with PBS 3 times, the fixed neurons were directly for
608 immunostaining following same staining protocol described above. Cultured neurons were
609 imaged with acquired using the ECLIPSE Ti2 inverted microscope.

610 Whole-mount DRG immunostaining was performed by injecting 0.1 μL of Lycopersicon
611 Esculentum Lectin (Vector, Catalog# DL-1178-1) through the tail vein to label the blood vessels
612 (Robertson et al., 2015). L4 DRGs were dissected after 20 minutes and fixed overnight in 4% PFA
613 at 4°C. Following a previously established protocol (Yang et al., 2017), DRGs underwent a series
614 of washing and permeabilization steps with 0.3% Triton X-100 in PBS, repeated every hour for 5

615 hours. Subsequently, the tissues were incubated with primary antibodies in a blocking solution
616 consisting of 75% 0.3% PBST, 20% DMSO, and 5% Donkey Serum for 4 days, followed by further
617 washing with 0.3% Triton X-100 in PBS every hour for 5 hours. The tissues were then incubated
618 with secondary antibodies in the blocking solution for 2 days, with subsequent washing using 0.3%
619 Triton X-100 in PBS every hour for 5 hours. All of these washing and incubation procedures were
620 carried out on a rocking platform at room temperature. The tissues were dehydrated in methanol
621 for 1 hour and cleared using a 1:2 mixture of Benzyl Alcohol to Benzyl Benzoate. Imaging was
622 carried out using an LSM880 confocal microscope, and blood vessel reconstruction was
623 performed with Imaris 9.7.

624 Primary antibodies included rabbit anti-FABP7 (Invitrogen, Catalog#:PA5-24949, 1:1000);
625 rabbit anti-STMN2(SCG10) (Novus a bio-techne, Catalog#:NBP1-49461, 1:1000); rabbit anti-
626 Connexin-43 (Cell Signaling, Catalog#: 3512s, 1:200); mouse anti TUJ1 (β-III tubulin) (Biolegend,
627 Catalog#:801202, 1:1000). Secondary antibodies conjugated to Alexa Fluor 488, Alexa Fluor 594
628 and Alexa Fluor 647 (Invitrogen), conjugated Fab Fragment Donkey anti Rabbit Alexa Fluor
629 (Jackson ImmunoResearch Labs) were diluted 1:500.

630 For intraepidermal nerve fibers density measurements, fixed, free floating 50-μm thick
631 sections of footpads from the hind limbs were stained with rabbit anti-Protein Gene Product 9.5
632 (1:500, ISBIO, Cat# LS-B5981-50), followed by AF594 conjugated secondary antibody (1:500,
633 Invitrogen, Cat# A-21207). Sections were mounted and coverslipped using VECTASHIELD anti-
634 fade mounting media with DAPI (Vector Laboratory, Cat# H-2000). PGP 9.5 positive
635 intraepidermal nerve fibers (IENFs) crossing into the epidermis were counted from Z-stack images
636 using the 20x objective on a Nikon W1 CSU SoRa. IENF densities were averaged from three to
637 four sections for each animal. Counting was performed with the observer blinded to the treatment
638 group.

639

640 **RNAscope® in situ hybridization**

641 The RNAscope® fluorescent multiplex reagent kit (Advanced Cell Diagnostics, ACD) was
642 used according to the manufacturer's instructions. Slides were retrieved from a -80°C freezer,
643 washed with PBS to remove OCT, and dried on a 60°C slide warmer for 5 minutes. Post-fixation
644 was performed by immersing the slides in cold (4°C) 4% paraformaldehyde (PFA) for 15 minutes.
645 Tissues were dehydrated using a series of ethanol washes (50% ethanol for 5 minutes, 70%
646 ethanol for 5 minutes, and 100% ethanol for 10 minutes) at room temperature. Slides were air
647 dried briefly and then incubated in RNAscope® Target Retrieval buffer (ACD; Catalog# 322000)
648 at 98-100°C for 5 minutes. After rinsing in 100% ethanol, hydrophobic boundaries were drawn
649 around each section using a hydrophobic pen (ImmEdge PAP pen; Vector Labs). Once the
650 boundaries were dry, protease III reagent was added to each section and incubated for 15 minutes.
651 Slides were briefly washed in PBS at room temperature. Each slide was placed in a prewarmed
652 humidity control tray (ACD) with dampened filter paper, and a mixture of probes was pipetted onto
653 each section until fully submerged. The slides were then incubated in a HybEZ oven (ACD) at
654 40°C for 2 hours. Following the probe incubation, the slides were washed twice with 1x RNAscope
655 wash buffer and returned to the oven for 30 minutes after submersion in AMP-1 reagent. This
656 washing and amplification process was repeated using AMP-2, AMP-3, and AMP-4 reagents with
657 incubation periods of 15 minutes, 30 minutes, and 15 minutes, respectively. For all mouse
658 experiments, AMP-4 ALT A (Channel 1 = Atto 488, Channel 2 = Alexa 550, Channel 3 = Atto 647)
659 was used. Slides were then washed twice with 0.1M phosphate buffer (PB, pH 7.4). Subsequently,
660 the slides were processed with 300nM DAPI at room temperature for 10 minutes and cover-
661 slipped using Prolong Gold Antifade mounting medium. DRG sections were imaged using a
662 confocal laser-scanning microscope (Zeiss LSM880).

663

664

665 **Transmission electron microscopy**

666 For transmission electron microscopy (TEM), mice were perfused PBS and then with the
667 fixative (2.5% glutaraldehyde and 4% paraformaldehyde in 0.1 M Cacodylate buffer), followed by
668 post-fixation in same fixation 24hrs at 4C. For secondary post fixation, the samples were rinsed
669 in 0.15 M cacodylate buffer containing 2mM calcium chloride 3 times for 10 minutes each followed
670 by a secondary fixation in 1% osmium tetroxide and 1.5% potassium ferrocyanide in 0.15 M
671 cacodylate buffer containing 2 mM calcium chloride for 1 hour in the dark. The samples were then
672 rinsed 3 times for 10 minutes each in ultrapure water and en bloc stained with 2% aqueous uranyl
673 acetate overnight at 4 °C in the dark. After 4 washes for 10 minutes each in ultrapure water, the
674 samples were dehydrated in a graded acetone series (10%, 30%, 50%, 70%, 90%, 100% x3) for
675 10 minutes each step, infiltrated with Spurr's resin (Electron Microscopy Sciences) and embedded
676 and polymerized at 60 °C for 72 hours. The samples from adult mice were processed as above
677 except they were dehydrated in a graded ethanol series (10%, 30%, 50%, 70%, 90%, 100% x3)
678 for 10 minutes each step, infiltrated with Epon resin (Electron Microscopy Sciences) and
679 embedded and polymerized at 60 °C for 48 hours. Post curing, 70 nm thin sections were cut,
680 post-stained with 2% aqueous uranyl acetate and Sato's lead and imaged on a TEM (Jeol JEM-
681 1400 Plus) at 120 kV.

682 **Single Cell RNA sequencing**

683 L4 and L5 DRGs from mice were collected and placed into cold dissection medium
684 consisting of Hank's Balanced Salt Solution (HBSS; ThermoFisher, Gibco; Catalog#: 14175-079)
685 supplemented with 10% 1M HEPES (ThermoFisher, Gibco; Catalog#: 15630080). Subsequently,
686 the ganglia were transferred to freshly prepared pre-warmed dissociation medium composed of
687 15 U/mL Papain suspension (Worthington Biochemical; Catalog#: LS003126), 0.3 mg/mL L-
688 cysteine (Sigma; Catalog#: C7352), 0.1 mg/mL Deoxyribonuclease I (Worthington Biochemical;
689 Catalog#: LS002139), and 10% 1M HEPES in HBSS. The samples were then incubated at 37°C

690 for 20 minutes. After two washes with pre-warmed HBSS, the ganglia were incubated with
691 collagenase (150 µg/mL; Sigma; Catalog#: C6885) at 37°C for 20 minutes. Following an additional
692 two washes with pre-warmed HBSS, the resulting single cell suspension was resuspended by
693 gently triturating in complete medium consisting of Neurobasal™-A Medium (ThermoFisher,
694 Gibco; Catalog#: 12349015) supplemented with B-27™ Plus Supplement (ThermoFisher, Gibco;
695 Catalog#: A3582801) and GlutaMAX™ Supplement (ThermoFisher, Gibco; Catalog#: 35050061).
696 The cell suspension was then passed through 70-micron cell strainers. The single cell suspension
697 was further resuspended in HBSS containing 10% 1M HEPES and 0.1% Fetal Bovine Serum
698 (FBS; ThermoFisher; Catalog#: A3160401). The cells were stained with the LIVE/DEAD™ Fixable
699 Aqua Dead Cell Stain Kit (ThermoFisher; Catalog#: L34965) to identify live cells. Live single cells
700 were sorted using the MoFlo cell sorter (Beckman Coulter, Indianapolis, IN). The sorted cells were
701 washed with a PBS+0.04% BSA solution and manually counted using a hemocytometer. The cell
702 solution was adjusted to a concentration of 700-1000 cells/µL and loaded onto the 10X Chromium
703 system.

704 Single-cell RNA-Seq libraries were prepared using the Chromium Next GEM Single Cell
705 3' (v3.1 Kit) from 10X Genomics. Read alignment and transcript counting were performed with
706 the CellRanger (v7.1.0) package from 10X Genomics and 19,356 cells with >300 detected genes
707 were retained for downstream analysis. Sample QC, principal component analysis, clustering,
708 DGE, quantification, and statistical analysis were performed using the Seurat package (v5.1.0).
709 Following normalization with SCTransform, principal component analysis, and graph-based
710 clustering, four low quality and/or doublet clusters were identified and removed based on the
711 following characteristics: statistical enrichment (DGE $p < 0.05$) of mixed major cell type marker
712 genes or mitochondria-specific transcripts, and/or low average genes per cell (<1000). After
713 removal of low-quality clusters, cells with disproportionately high mitochondrial transcript levels
714 (calculated as the fraction of reads mapping to mitochondrial genes) or UMI counts were filtered

715 by setting a cutoff at the median plus five median absolute deviations (MAD) for each metric. The
716 remaining 16,764 high-quality cells were visualized using UMAP (Uniform Manifold Approximation
717 and Projection). Differential gene expression (DGE) analyses were performed in the Seurat
718 package with a Wilcoxon Rank Sum test, and genes with Bonferroni-adjusted p-values < 0.05
719 were considered for downstream analysis and visualization.

720 **Single Nucleus RNA sequencing**

721 L3, L4 and L5 DRGs were collected from mice and immediately placed on dry ice. DRG
722 were stored in -80 until processing. Nuclei were isolated using the Illumina Nuclei Isolation Kit
723 (Illumina; Catalog# 20132795). The DRG were dissociated using a KIMBLE 2mL Dounce
724 homogenizer (Sigma; Catalog# D8938) in Nuclei Extraction Buffer (NEB) and passed through a
725 40-micron cell strainer. The nuclei were briefly centrifuged and then passed through a 10-micron
726 cell strainer. The nuclei were resuspended in Nuclei Suspension Buffer (NSB) and counted for
727 intact nuclei using 7-AAD stain (Sigma; Catalog# SML1633). Nuclei were processed using the
728 Illumina Single Cell 3' RNA Prep, T20 Kit (Illumina; Catalog# FB0005366, FB0005373,
729 FB0005362, FB0005382)

730 Single-nuclei RNA-Seq libraries were prepared using the Illumina V Library Prep Kit
731 (Illumina; Catalog# 20132789, FB0005374, FB0005373). Read alignment and transcript counting
732 were performed with the Pipseeker (v3.3.0) package from Fluent BioSciences and 19,270 cells
733 with >1000 genes were retained for downstream analysis (11,521 adult, 7,749 aged). Sample QC,
734 integration, clustering, DGE, quantification, and statistical analysis were performed using the
735 Seurat package (v5.1.0). Following normalization with SCTransform, RPCA batch integration, and
736 graph-based clustering, five low quality and/or doublet clusters were identified and removed
737 based on the following characteristics: statistical enrichment (DGE p < 0.05) of mixed major cell
738 type marker genes or mitochondria-specific transcripts, and/or low total cell count (<50). The
739 remaining 17,852 high-quality cells were visualized using UMAP. Differential gene expression

740 (DGE) analyses were performed in the Seurat package with a Wilcoxon Rank Sum test, and
741 genes with Bonferroni-adjusted p-values < 0.05 were considered for downstream analysis and
742 visualization. KEGG pathway and GO enrichment were performed using the clusterProfiler
743 package in R. The researcher was not blinded during analysis.

744 **Images acquisition and quantification**

745 Confocal images were captured under the LSM880 confocal microscope (Carl Zeiss)
746 unless otherwise specified. The images were captured under following parameters: 1 × optical
747 zoom, scan speed 6, averaged 2 times, a pinhole of 1 AU, 1024 × 1024 pixel size. The z-stack
748 images were projected into overlay images using the "Maximum Intensity Projection" function in
749 Zen Black software (Carl Zeiss). Sciatic nerve longitudinal images, the spinal cord and brain
750 images were captured under the EVOS™ M7000 Imaging System (Invitrogen). The images were
751 captured under 10x objective in 1980 × 1080 pixel size. The stitched nerve images generated by
752 the EVOS imaging system. The neuronal culture images were captured under the ECLIPSE Ti2
753 inverted microscope (Nikon). The images were captured under 10x objective in 2304 × 2304 pixel
754 size. Three tissue sections were analyzed on average for each independent mouse. The
755 researcher performing this analysis was not blinded during analysis.

756 For quantifying Cx43 expression area in the DRG, the $CX43^+$ and $Fabp7^+$ area was
757 measured using "Analysis Particles" function in Fiji. To quantify CX43, confocal imaging with Z-
758 stacks (10 μm) was performed using an LSM880 microscope. The acquired images were
759 subsequently used for 3D reconstruction using Imaris 9.7 software. The staining area of FABP7
760 underwent initial surface reconstruction, while the CX43 puncta were isolated through spot
761 reconstruction at a resolution of 0.1 μm x 0.2 μm. The average number of CX43 puncta was
762 determined for each $FABP7^+$ cell (Supplementary Video S1). For quantifying the regeneration
763 index in the injured sciatic nerve section, the highest SCG10 intensity along the nerve was defined
764 as the crush site, as described (Cho et al., 2013; Feng et al., 2023). The average SCG10 intensity

765 at distances away from the crush site was normalized to the SCG10 intensity at the crush site
766 using “measure” function in Fiji. For quantifying the neuron regenerative capacity in cultured DRG
767 neurons, TUJ1 stained neurons were segmented by thresholding and subjected to neurite tracing
768 using “Simple Neurite Tracer” plug-in in Fiji. The researcher was not blinded during analysis.

769 DRG explant analysis was performed by creation of an ROI around each explant. The ROI
770 was removed for organoid contrast and the radial length was measured from the outer peripheral
771 section of the ROI. The 35 longest axons in each image were measured (μm) and averaged.

772 For TEM, SGCs width around the neuron was measured by averaging 4 individual points
773 that did not contain an SGCs nucleus around the neuron using Fiji/ImageJ software. Frequency
774 of neurons with 0,1,2, or 3 SGCs nuclei per neuron was quantified by counting each image by
775 eye.

776 **Statistical analysis**

777 All statistical analyses and graphs were conducted, organized and generated in GraphPad
778 Prism 9. Numerical data were presented as mean ± SD from at least three independent animals.
779 Group mean difference was analyzed by either two-tailed unpaired Student’s t-test or one-way
780 ANOVA with Bonferroni post-hoc test. For experiments including groups and multiple time-point
781 measurements, data were analyzed by two-way ANOVA with Bonferroni post-hoc test. P values
782 below 0.05 were considered as significant difference. The number of animals in each group is
783 presented in figure legends. No a priori exclusion criteria or statistical power calculations were
784 used.

785 **Data and materials availability:**

786 All data associated with this study are presented in the paper or the Supplementary
787 Materials. scRNA and snRNA sequencing data have been deposited at NCBI Gene Expression
788 Omnibus (GEO) under accession number GSE298413 (reviewer token: yjajwmuyrxytfqj) and
789 GSE298412 (reviewer token: mxmpsaqkpxwtdsd).

790 **List of Supplementary Materials**

791 Supplementary Figures S1 to S6

792 Supplementary Data File S1 to S5

793 Supplementary Movie S1 and S2

794

795 **Acknowledgments:**

796 We would like to thank members of the Cavalli lab and the Mokalled lab for valuable
797 discussions and suggestions. We gratefully acknowledge Michael Savio from The Alvin J.
798 Siteman Cancer Center at Barnes-Jewish Hospital and Washington University School of Medicine
799 for assistance with single cell sorting. We also acknowledge the assistance of John Wulf II,
800 Gregory Strout and Dr. Sanja Sviben at the Washington University Center for Cellular Imaging
801 (WUCCI) in electron microscopy studies, which is supported by Washington University School of
802 Medicine, The Children's Discovery Institute of Washington University and St. Louis Children's
803 Hospital (CDI-CORE-2015-505 and CDI-CORE-2019-813) and the Foundation for Barnes-Jewish
804 Hospital (3770 and 4642). TEM images were acquired using an AMT Nanosprint15-MkII sCMOS
805 camera, which was purchased with support from the Office of Research Infrastructure Programs
806 (ORIP), a part of the NIH Office of the Director under grant (OD032186). The authors show their
807 gratitude and respect to all animals sacrificed in this study.

808 **Funding:**

809 This work was funded in part by NIH grants R35 NS122260, R01 NS111719 and R21
810 NS115492 to V.C.

811 **Author contributions:**

812 R.F. and V.C. conceptualized the study, C.G and V.C. provided study supervision. R.F.,
813 S.F.R, S.J., I.A. and O.A performed experiments and analyzed data. R.F., S.F.R, S.J. and I.A.

generated figures and visualizations. M.B.T performed bioinformatics analyses. R.F., S.F.R and V.C. wrote the manuscript and all authors edited the manuscript.

Competing interests:

V. C and R.F are inventors on a patent application related to this work

FIGURES LEGENDS

Figure 1: *Ednrb* is highly expressed in satellite glial cells.

A. Representative whole-mount-stained images of DRG from Lycopersicon Esculentum Lectin (LEL) injected Fabp7CreER::Ai14 mice, labeled for TUJ1 (green), tdTomato (magenta), and LEL (grey). 3D reconstruction of blood vessels via LEL labeling (scale bars, 200 μm)**.** Note that TUJ1 antibody staining is limited by penetration of the antibody in the whole mount.

B. Representative images of sectioned DRG from Lycopersicon Esculentum Lectin (LEL) injected C57BL/6 mice, labeled for TUJ1 (green), Fabp7 (red), and LEL (cyan) (Scale bars, 100 μm).

C. UMAP analysis of adult DRG 10X sequencing data identified 8 cell clusters based on known marker genes.

D. Dot plot analysis showing the average gene expression (color coded) and number of expressing cells (dot size) for the marker genes.

E-H. UMAP overlay for expression of *Ednra* (**E**), *Ednrb* (**F**), *Edn1* (**G)** and *Edn3* (**H**).

I. Representative RNAScope *in situ* hybridization images showing *Ednrb* (red), *Fabp7* (cyan) and DAPI (blue) of L4 DRGs from 3-month-old mice (scale bars, 50 μm).

Figure 2: Endothelin B receptor inhibition increases axonal growth *in vitro* and *ex vivo.*

A. Representative images showing TUJ1 (black) immunostaining of neurons in DRG cultures (scale bars, 100 μm).

B. Representative image of TUJ1 (green) and FABP7 (magenta) immunostaining of neurons and SGCs in control DRG cultures (scale bars, 50 μm).

C,D. Quantification of axonal radial length (B) and $TUJ1^+$ area (C) per neuron. Different colors indicate biological replicates. N = 246 (Veh; 8 replicates), 318 (BQ788; 8 replicates), 320 (IRL1620; 8 replicates), and 244 (BQ123; 8 replicates). Data presented as mean ± SD.

E. Scheme of drug treatment and DRG explant model.

F. Representative images of DRG explants 7 days after drug treatment, immunostained for TUJ1 (black) (scale bars, 1000 μm).

G. Quantification of radial length of the 35 longest axons from DRG explants from indicated groups N=36 explants from 6 indivual mice (BQ788; 18 replicates, Veh; 18 replicates).

H. Representative images of DRG explants immunostained for TUJ1 (green), FABP7 (magenta), and merged (scale bars, 50 μm).

852 **Figure 3: Bosentan treatment improves axon regeneration after peripheral nerve injury in**
853 **adult mice.**
854 **A.** Scheme of drug treatment and peripheral nerve injury model.
855 **B.** Quantification of the length of the 10 longest axons in indicated conditions.
856 **C**. Quantification of the regeneration index, calculated as the distance along the nerve where
857 the SGC10 intensity is 50% of the SCG10 intensity at crush site.
858 **D.** Representative longitudinal sections of sciatic nerves 24h after SNC, immunostained for
859 SCG10, from mice with the indicated treatment. Dotted line indicates the crush site, determined
860 as the maximal SGC10 intensity (scale bars, 200 μm).
861 **E.** Quantificaiton of SCG10 intensity at the indicated distance normalized to the intensity at the
862 crush site for each condition. N = 5 mice/condition.
863 **F**. Scheme of long-term Bosentan treatment.
864 **G**. Representative images of hindpaw skin after long-term Bosentan treatment immunostained
865 for PGP9.5 (white) and DAPI (blue) (scale bars, 50 μm).
866 **H**. Quantification of intraepidermal nerve fiber density (IENFD) 24 days after sciatic nerve crush
867 from the indicated groups. N=5 mice/condition.
868 **I.** Scheme of adult DRG neuronal culture and treatments.
869 **J,L.** Representative images showing TUJ1 (black) immunostaining of neurons in DRG cultures
870 (scale bars, 100 μm).
871 **K,M.** Quantification of axonal radial length (K) and total $TUJ1^+$ area (L). Different colors
872 represent different biological replicates. N (neuron number) = 177 (vehicle; three biological
873 replicates, naïve mice), 168 (Ambrisentan, three biological replicates, naïve mice), 183
874 (Bosentan; three biological replicates, naïve mice), 186 (vehicle; three biological replicates,
875 injured mice), 204(Ambrisentan, three biological replicates, injured mice) and 210 (Bosentan;
876 three biological replicates, injured mice), respectively. The data are presented as mean ± SD.
877
878 **Figure 4: Bosentan treatment rescues aging-dependent neuronal regenerative decline.**
879 **A.** Scheme of drug treatment and DRG explant model.
880 **B.** Representative images of DRG explants 7 days after drug treatment (scale bars, 1000 μm).
881 **C.** Quantification of radial length of the 50 longest axons from DRG explants. N=36 explants
882 from 6 indivual mice (BQ788; 18 replicates, Veh; 18 replicates).
883 **D.** Representative longitudinal sections of sciatic nerves 3 d after SNC immunostained for
884 SCG10 from mice with the indicated treatment. Dotted line indicates the crush site, determined
885 as the maximal SCG10 intensity (scale bars, 200 μm).

886 **E,F.** Quantification of the 10 longest axons in indicated groups (**E**). Quantificaiton of 50%
887 regenerative index, calculated as the disatnce along the nerve where the SCG10 intensity is
888 50% of the SCG10 intensity at crush site (**F**).
889 **G.** Quantification of the SCG10 intensity at the indicated distance normalized to the intensity at
890 the crush site for each condition. N (mouse number) = 4(adult, vehicle), 3 (Aged, vehicle) and 3
891 (Bosentan+Age), respectively. The data are presented as mean ± SD.
892
893 **Figure 5: Aging alters SGC abundance and morphology.**
894 **A.** UMAP plot of adult and aged snRNA-seq identified 16 cell clusters based on known marker
895 genes.
896 **B.** Dot plot analysis showing the average gene expression (color coded) and number of
897 expressing cells (dot size) for the marker genes.
898 **C,D.** UMAP plot of DRG cells from adult (**C**) and aged (**D**) mice.
899 **E.** Bar plot of cell proportions in DRGs of adult and aged mice.
900 **F.** Representative TEM images of DRG sections from adult (2M), middle aged (12M) and aged
901 (21M) mice showing neuronal cell bodies and the enveloping SGCs (SGCs are pseudo-colored
902 in red) (scale bars, 5 μm).
903 **G.** Quantification of the average width of SGCs sheath per neuron soma.
904 **H.** Frequency of neurons soma in TEM images with 0, 1, 2, or 3 SGCs nuclei in 2M, 12M, and
905 21M old mice.
906
907
908 **Figure 6: ETBR inhibition increases the expression of Cx43 in SGCs in adult and aged**
909 **mice.**
910 **A.** UMAP overlay for expression of *Gja1* in adult and aged mouse DRG.
911 **B.** Scheme of drug treatment and peripheral nerve injury model.
912 **C.** Quantification of the percentage of the Cx43/FABP7 expression area.
913 **D.** Quantification of the average number of Connexin 43 (Cx43) puncta per FABP7+ cell. The
914 ratio of total Cx43 puncta to the number of FABP7+ cells surrounding a TUJ1+ neuron was
915 measured. N(cell number) = 60(adult, uninjured), 62(aged, uninjured), 96(vehicle, adult, SNC),
916 117(bosentan, adult, SNC), 74(vehicle, aged, SNC) and 74(bosentan, aged, SNC), respectively.
917 **E.** Representative immunostaining images showing Connexin 43 (Cx43), FABP7 and TUJ1 in
918 L4 DRGs from the indicated condition (scale bars, 50 μm).
919 **F.** Proposed model for the role of ETBR in age-dependent decline in axon regenerative capacity

920 **SUPPLEMENTARY FIGURES**

921

922 **Figure 1 – Figure supplement 1.**

923 **A,B.** Sample QC for 10x scRNA-Seq

924 **C.** UMAP plots of genes used for cell cluster annotations.

925 **D.** UMAP overlay for expression of *Ednrb* in SGCs in mouse and human. Images generated

926 from https://painseq.shinyapps.io/harmonized_painseq_v2/, related to (Bhuiyan et al., 2024).

927

928 **Figure 3 – Figure supplement 1**

929 **A.** Scheme of drug treatment and peripheral nerve injury model.

930 **B.** Quantification of the 10 longest axons in indicated groups.

931 **C.** Quantificaiton of 50% regenerative index, calculated as the disatnce along the nerve where

932 the SCG10 intensity is 50% of the SCG10 intensity at crush site.

933 **D.** Representative longitudinal sections of sciatic nerves 3 d after SNC immunostained for

934 SCG10 from mice with the indicated treatment. Dotted line indicates the crush site, determined

935 as the maximal SCG10 intensity (scale bars, 200 μm).

936 **E.** Quantificaiton of SCG10 intensity at the indicated distance normalized to the intensity at the

937 crush site for each condition. N = 5 mice/condition. The data are presented as mean ± SD.

938 **F.** RT-qPCR of *Atf3, Aif1, Fabp7, Edn1, Ednra* and *Ednrb* gene in contralateral (CON) and

939 ipsilateral DRGs at 3days post injury(SNC). N (mouse number) = 4/each group.

940 **G.** Western blot analysis and quantification of ETBR protein expression in DRGs from the mice

941 with/without injury.

942 **H.** Quantification of ETBR expression normalized to GAPDH expression (folder of control mice).

943 N (mouse number) = 8/group. The data are presented as mean ± SD.

944

945 **Figure 3 – Figure supplement 2**

946 **A.** Scheme of drug treatment and dorsal root crush injury model.

947 **B.** Representative longitudinal sections of sciatic nerves 3 d after DRC immunostained for

948 SCG10 from mice with the indicated treatment. Dotted line indicates the crush site, determined

949 as the maximal SCG10 intensity (scale bars, 200 μm).

950 **C.** Quantification of the 10 longest axons in indicated groups.

951 **D.** Quantificaiton of 50% regenerative index, calculated as the disatnce along the nerve where

952 the SCG10 intensity is 50% of the SCG10 intensity at crush site.

953 **E.** Quantificaiton of SCG10 intensity at the indicated distance normalized to the intensity at the
954 crush site for each condition. N = 5 mice/condition. The data are presented as mean ± SD.
955
956 **Figure 4 – Figure supplement 1**
957 **A,B.** Western blot analysis and quantifiction of ET1 (A) and ETBR (B) protein expression in
958 DRG from adult and aged mice N=3 for each age group.
959 **C.** Scheme of drug treatment and explant culture model.
960 **D.** Quantification of radial length of the 10 longest axons from DRG explants. N=20 (Bosentan;
961 9 replicates, Veh; 11 replicates)
962 **E.** Representative images of DRG explants 4 days after culture (scale bars, 1000 μm).
963
964 **Figure 5 – Figure supplement 1**
965 **A,B.** Sample QC for Illumina snRNA-Seq
966 **C.** Volcano plot of upregulated and downregulated genes in SGCs of aged vs. adult mice.
967 **D.** Gene ontology analysis of upregulated genes in SGCs in aged mice compared to adults.
968
969 **Figure 6 – Figure supplement 1**
970 **A.** Representative immunostaining images of connexin 43 (red), Fabp7 (gray), and TUJ1 (cyan)
971 in L4 DRGs from mice of the indicated ages and treatments 3 d after dorsal root crush injury
972 (scale bars, 50 μm).
973 **B.** Quantification of the percentage of the Cx43/FABP7 expression area in each condition.
974 **C.** Quantification of the average number of Connexin 43 (Cx43) puncta per FABP7^{+} cell. The
975 ratio of total Cx43 puncta to the number of FABP7^{+} cells surrounding a TUJ1-positive neuron
976 was measured. Different colors were used to indicate distinct biological replicates (mouse).
977 N(cell number) = 93 (uninjured), 97 (Vehicle, DRC), and 124 (Bosentan, DRC), respectively.
978 The data are presented as mean ± SD.
979
980 **SUPPLEMENTARY DATA FILES**
981 **S1:**Marker genes for 10x scRNA-seq analysis
982 **S2:**Marker genes for Illumina snRNA-seq analysis
983 **S3:**DGE for SGCs in aged vs adult DRG
984 **S4:**GO pathway analysis for SGC in aged vs adult DRG
985 **S5:** KEGG pathway analysis for SGC is aged vs adult DRG
986

987 **SUPPLEMENTARY TABLES**

988 **Supplementary Table 1:** list of qPCR Primers

989

990 **SUPPLEMENTARY MOVIES**

991 **Movie S1:** Z-stack video of whole mount preparation of DRG from Lycopersicon Esculentum
992 Lectin (LEL) injected Fabp7CreER::Ai14 mouse, which labels SGCs with tdTomato,
993 immunostained for TUJ1 (neurons).

994

995 **Movie S2:** Z-stack video of DRG section immunostained for FABP7 and CX43.

996

997 **REFERENCES**

998 Aldskogius, H., and M. Risling. 1989. Number of dorsal root ganglion neurons and axons in cats
999 of different ages. *Experimental neurology*. 106:70-73.

1000 Andrews, M.R., S. Soleman, M. Cheah, D.A. Tumbarello, M.R. Mason, E. Moloney, J. Verhaagen,
1001 J.C. Bensadoun, B. Schneider, P. Aebischer, and J.W. Fawcett. 2016. Axonal Localization
1002 of Integrins in the CNS Is Neuronal Type and Age Dependent. *eNeuro*. 3.

1003 Avraham, O., A. Chamessian, R. Feng, L. Yang, A.E. Halevi, A.M. Moore, R.W.t. Gereau, and V.
1004 Cavalli. 2022. Profiling the molecular signature of satellite glial cells at the single cell level
1005 reveals high similarities between rodents and humans. *Pain*. 163:2348-2364.

1006 Avraham, O., P.Y. Deng, S. Jones, R. Kuruvilla, C.F. Semenkovich, V.A. Klyachko, and V. Cavalli.
1007 2020. Satellite glial cells promote regenerative growth in sensory neurons. *Nat Commun*.
1008 11:4891.

1009 Avraham, O., R. Feng, E.E. Ewan, J. Rustenhoven, G. Zhao, and V. Cavalli. 2021. Profiling
1010 sensory neuron microenvironment after peripheral and central axon injury reveals key
1011 pathways for neural repair. *Elife*. 10.

1012 Barton, M. 2014. Aging and endothelin: determinants of disease. *Life Sci*. 118:97-109.

1013 Belzer, V., N. Shraer, and M. Hanani. 2010. Phenotypic changes in satellite glial cells in cultured
1014 trigeminal ganglia. *Neuron glia biology*. 6:237-243.

1015 Berger, U.V., and M.A. Hediger. 2000. Distribution of the glutamate transporters GLAST and GLT-
1016 1 in rat circumventricular organs, meninges, and dorsal root ganglia. *The Journal of*
1017 *comparative neurology*. 421:385-399.

1018 Bhat, G.P., A. Maurizio, A. Motta, P. Podini, S. Diprima, C. Malpighi, I. Brambilla, L. Martins, A.
1019 Badaloni, D. Boselli, F. Bianchi, M. Pellegatta, M. Genua, R. Ostuni, U. Del Carro, C.
1020 Taveggia, S. de Pretis, A. Quattrini, and D. Bonanomi. 2024. Structured wound
1021 angiogenesis instructs mesenchymal barrier compartments in the regenerating nerve.
1022 *Neuron*. 112:209-229 e211.

1023 Bhuiyan, S.A., M. Xu, L. Yang, E. Semizoglou, P. Bhatia, K.I. Pantaleo, I. Tochitsky, A. Jain, B.
1024 Erdogan, S. Blair, V. Cat, J.M. Mwirigi, I. Sankaranarayanan, D. Tavares-Ferreira, U.
1025 Green, L.A. McIlvried, B.A. Copits, Z. Bertels, J.S. Del Rosario, A.J. Widman, R.A. Slivicki,
1026 J. Yi, R. Sharif-Naeini, C.J. Woolf, J.K. Lennerz, J.L. Whited, T.J. Price, W.G.I. Robert,
1027 and W. Renthal. 2024. Harmonized cross-species cell atlases of trigeminal and dorsal root
1028 ganglia. *Sci Adv*. 10:eadj9173.

1029 Black, M.M., and R.J. Lasek. 1979. Slowing of the rate of axonal regeneration during growth and
1030 maturation. *Experimental neurology*. 63:108-119.

1031 Blomstrand, F., L. Venance, A.L. Siren, P. Ezan, E. Hanse, J. Glowinski, H. Ehrenreich, and C.
1032 Giaume. 2004. Endothelins regulate astrocyte gap junctions in rat hippocampal slices. *The*
1033 *European journal of neuroscience*. 19:1005-1015.

1034 Brennan, A., C.H. Dean, A.L. Zhang, D.T. Cass, R. Mirsky, and K.R. Jessen. 2000. Endothelins
1035 control the timing of Schwann cell generation in vitro and in vivo. *Developmental biology*.
1036 227:545-557.

1037 Buttner, R., A. Schulz, M. Reuter, A.K. Akula, T. Mindos, A. Carlstedt, L.B. Riecken, S.L. Baader,
1038 R. Bauer, and H. Morrison. 2018. Inflammaging impairs peripheral nerve maintenance and
1039 regeneration. *Aging Cell*. 17:e12833.

1040 Carlin, D., A.E. Halevi, E.E. Ewan, A.M. Moore, and V. Cavalli. 2019. Nociceptor Deletion of Tsc2
1041 Enhances Axon Regeneration by Inducing a Conditioning Injury Response in Dorsal Root
1042 Ganglia. *eNeuro*. 6.

1043 Cattin, A.L., J.J. Burden, L. Van Emmenis, F.E. Mackenzie, J.J. Hoving, N. Garcia Calavia, Y.
1044 Guo, M. McLaughlin, L.H. Rosenberg, V. Quereda, D. Jamecna, I. Napoli, S. Parrinello, T.
1045 Enver, C. Ruhrberg, and A.C. Lloyd. 2015. Macrophage-Induced Blood Vessels Guide
1046 Schwann Cell-Mediated Regeneration of Peripheral Nerves. *Cell*. 162:1127-1139.

1047 Chen, S., M.D. Apostolova, M.G. Cherian, and S. Chakrabarti. 2000. Interaction of endothelin-1
1048 with vasoactive factors in mediating glucose-induced increased permeability in endothelial
1049 cells. *Lab Invest*. 80:1311-1321.

1050 Chen, X., Z. Zhai, K. Huang, W. Xie, J. Wan, and C. Wang. 2018. Bosentan therapy for pulmonary
1051 arterial hypertension and chronic thromboembolic pulmonary hypertension: A systemic
1052 review and meta-analysis. *Clin Respir J*. 12:2065-2074.

1053 Cho, Y., and V. Cavalli. 2012. HDAC5 is a novel injury-regulated tubulin deacetylase controlling
1054 axon regeneration. *EMBO J*. 31:3063-3078.

1055 Cho, Y., J.E. Shin, E.E. Ewan, Y.M. Oh, W. Pita-Thomas, and V. Cavalli. 2015. Activating Injury-
1056 Responsive Genes with Hypoxia Enhances Axon Regeneration through Neuronal HIF-
1057 1alpha. *Neuron*. 88:720-734.

1058 Cho, Y., R. Sloutsky, K.M. Naegle, and V. Cavalli. 2013. Injury-induced HDAC5 nuclear export is
1059 essential for axon regeneration. *Cell*. 155:894-908.

1060 Clozel, M., V. Breu, G.A. Gray, B. Kalina, B.M. Loffler, K. Burri, J.M. Cassal, G. Hirth, M. Muller,
1061 W. Neidhart, and et al. 1994. Pharmacological characterization of bosentan, a new potent
1062 orally active nonpeptide endothelin receptor antagonist. *J Pharmacol Exp Ther*. 270:228-
1063 235.

1064 Costigan, M., J. Scholz, and C.J. Woolf. 2009. Neuropathic pain: a maladaptive response of the
1065 nervous system to damage. *Annu Rev Neurosci*. 32:1-32.

1066 Davenport, A.P., K.A. Hyndman, N. Dhaun, C. Southan, D.E. Kohan, J.S. Pollock, D.M. Pollock,
1067 D.J. Webb, and J.J. Maguire. 2016. Endothelin. *Pharmacol Rev*. 68:357-418.

1068 Feldman-Goriachnik, R., and M. Hanani. 2017. The effects of endothelin-1 on satellite glial cells
1069 in peripheral ganglia. *Neuropeptides*. 63:37-42.

1070 Feng, R., V. Muraleedharan Saraswathy, M.H. Mokalled, and V. Cavalli. 2023. Self-renewing
1071 macrophages in dorsal root ganglia contribute to promote nerve regeneration.
1072 *Proceedings of the National Academy of Sciences of the United States of America*.
1073 120:e2215906120.

1074 Frazel, P.W., K. Fricano-Kugler, A.A. May-Zhang, M.R. O'Dea, P. Prakash, N.M. Desmet, H. Lee,
1075 R.H. Meltzer, K.M. Fontanez, P. Hettige, Y. Agam, G. Lithwick-Yanai, D. Lipson, B.W.
1076 Luikart, J.D. Dasen, and S.A. Liddelow. 2023. Single-cell analysis of the nervous system
1077 at small and large scales with instant partitions. *bioRxiv*.

1078 Fuentes-Flores, A., C. Geronimo-Olvera, K. Girardi, D. Necunir-Ibarra, S.K. Patel, J. Bons, M.C.
1079 Wright, D. Geschwind, A. Hoke, J.A. Gomez-Sanchez, B. Schilling, D.L. Rebolledo, J.
1080 Campisi, and F.A. Court. 2023. Senescent Schwann cells induced by aging and chronic
1081 denervation impair axonal regeneration following peripheral nerve injury. *EMBO Mol Med*.
1082 15:e17907.

1083 Galie, N., H. Olschewski, R.J. Oudiz, F. Torres, A. Frost, H.A. Ghofrani, D.B. Badesch, M.D.
1084 McGoon, V.V. McLaughlin, E.B. Roecker, M.J. Gerber, C. Dufton, B.L. Wiens, L.J. Rubin,
1085 and R.D.-B.P.-C.M.E.S.G. Ambrisentan in Pulmonary Arterial Hypertension. 2008.
1086 Ambrisentan for the treatment of pulmonary arterial hypertension: results of the
1087 ambrisentan in pulmonary arterial hypertension, randomized, double-blind, placebo-
1088 controlled, multicenter, efficacy (ARIES) study 1 and 2. *Circulation*. 117:3010-3019.

1089 Geoffroy, C.G., B.J. Hilton, W. Tetzlaff, and B. Zheng. 2016. Evidence for an Age-Dependent
1090 Decline in Axon Regeneration in the Adult Mammalian Central Nervous System. *Cell*
1091 *reports*. 15:238-246.

1092 Geoffroy, C.G., J.M. Meves, and B. Zheng. 2017. The age factor in axonal repair after spinal cord
1093 injury: A focus on neuron-intrinsic mechanisms. *Neuroscience letters*. 652:41-49.

1094 Giaid, A., S.J. Gibson, B.N. Ibrahim, S. Legon, S.R. Bloom, M. Yanagisawa, T. Masaki, I.M.
1095 Varndell, and J.M. Polak. 1989. Endothelin 1, an endothelium-derived peptide, is
1096 expressed in neurons of the human spinal cord and dorsal root ganglia. *Proceedings of*
1097 *the National Academy of Sciences of the United States of America*. 86:7634-7638.

1098 Godel, T., M. Pham, S. Heiland, M. Bendszus, and P. Baumer. 2016. Human dorsal-root-ganglion
1099 perfusion measured in-vivo by MRI. *Neuroimage*. 141:81-87.

1100 Ham, D., W. Shihoya, O. Nureki, A. Inoue, and K.Y. Chung. 2024. Molecular mechanism of the
1101 endothelin receptor type B interactions with Gs, Gi, and Gq. *Structure*. 32:1632-1639
1102 e1634.

1103 Hanani, M., and D.C. Spray. 2020. Emerging importance of satellite glia in nervous system
1104 function and dysfunction. *Nat Rev Neurosci*. 21:485-498.

1105 Hanani, M., and A. Verkhratsky. 2021. Satellite Glial Cells and Astrocytes, a Comparative Review.
1106 *Neurochem Res*.

1107 He, Z., and Y. Jin. 2016. Intrinsic Control of Axon Regeneration. *Neuron*. 90:437-451.

1108 Hoke, A. 2006. Mechanisms of Disease: what factors limit the success of peripheral nerve
1109 regeneration in humans? *Nat Clin Pract Neurol*. 2:448-454.

1110 Huang, T.Y., P.S. Cherkas, D.W. Rosenthal, and M. Hanani. 2005. Dye coupling among satellite
1111 glial cells in mammalian dorsal root ganglia. *Brain research*. 1036:42-49.

1112 Huang, T.Y., M. Hanani, M. Ledda, S. De Palo, and E. Pannese. 2006. Aging is associated with
1113 an increase in dye coupling and in gap junction number in satellite glial cells of murine
1114 dorsal root ganglia. *Neuroscience*. 137:1185-1192.

1115 Humbert, M., O. Sitbon, and G. Simonneau. 2004. Treatment of pulmonary arterial hypertension.
1116 *N Engl J Med*. 351:1425-1436.

1117 Jager, S.E., L.T. Pallesen, M. Richner, P. Harley, Z. Hore, S. McMahon, F. Denk, and C.B.
1118 Vaegter. 2020. Changes in the transcriptional fingerprint of satellite glial cells following
1119 peripheral nerve injury. *Glia*.

1120 Jankowich, M., and G. Choudhary. 2020. Endothelin-1 levels and cardiovascular events. *Trends*
1121 *Cardiovasc Med*. 30:1-8.

1122 Jessen, K.R., and R. Mirsky. 2016. The repair Schwann cell and its function in regenerating
1123 nerves. *J Physiol*. 594:3521-3531.

1124 Jimenez-Andrade, J.M., M.B. Herrera, J.R. Ghilardi, M. Vardanyan, O.K. Melemedjian, and P.W.
1125 Mantyh. 2008. Vascularization of the dorsal root ganglia and peripheral nerve of the

1126 mouse: implications for chemical-induced peripheral sensory neuropathies. *Molecular*
1127 *pain*. 4:10.

1128 Jung, M., M. Dourado, J. Maksymetz, A. Jacobson, B.I. Laufer, M. Baca, O. Foreman, D.H.
1129 Hackos, L. Riol-Blanco, and J.S. Kaminker. 2023. Cross-species transcriptomic atlas of
1130 dorsal root ganglia reveals species-specific programs for sensory function. *Nat Commun*.
1131 14:366.

1132 Kang, H., and J.W. Lichtman. 2013. Motor axon regeneration and muscle reinnervation in young
1133 adult and aged animals. *The Journal of neuroscience : the official journal of the Society*
1134 *for Neuroscience*. 33:19480-19491.

1135 Kappes, L., R.L. Amer, S. Sommerlatte, G. Bashir, C. Plattfaut, F. Gieseler, T. Gemoll, H. Busch,
1136 A. Altahrawi, A. Al-Sbiei, S.M. Haneefa, K. Arafat, L.F. Schimke, N.E. Khawanky, K.
1137 Schulze-Forster, H. Heidecke, A. Kerstein-Staehle, G. Marschner, S. Pitann, H.D. Ochs,
1138 A. Mueller, S. Attoub, M.J. Fernandez-Cabezudo, G. Riemekasten, B.K. Al-Ramadi, and
1139 O. Cabral-Marques. 2020. Ambrisentan, an endothelin receptor type A-selective
1140 antagonist, inhibits cancer cell migration, invasion, and metastasis. *Scientific reports*.
1141 10:15931.

1142 Klimovich, P., K. Rubina, V. Sysoeva, and E. Semina. 2020. Three-Dimensional Model of Dorsal
1143 Root Ganglion Explant as a Method of Studying Neurotrophic Factors in Regenerative
1144 Medicine. *Biomedicines*. 8.

1145 Koyama, Y. 2021. Endothelin ET(B) Receptor-Mediated Astrocytic Activation: Pathological Roles
1146 in Brain Disorders. *Int J Mol Sci*. 22.

1147 Li, S., J.J. Overman, D. Katsman, S.V. Kozlov, C.J. Donnelly, J.L. Twiss, R.J. Giger, G. Coppola,
1148 D.H. Geschwind, and S.T. Carmichael. 2010. An age-related sprouting transcriptome
1149 provides molecular control of axonal sprouting after stroke. *Nature neuroscience*. 13:1496-
1150 1504.

1151 Lie, M., M. Grover, and D.S. Whitlon. 2010. Accelerated neurite growth from spiral ganglion
1152 neurons exposed to the Rho kinase inhibitor H-1152. *Neuroscience*. 169:855-862.

1153 Liu, W., R. Glueckert, F.H. Linthicum, G. Rieger, M. Blumer, M. Bitsche, E. Pechriggl, H. Rask-
1154 Andersen, and A. Schrott-Fischer. 2014. Possible role of gap junction intercellular
1155 channels and connexin 43 in satellite glial cells (SGCs) for preservation of human spiral
1156 ganglion neurons : A comparative study with clinical implications. *Cell Tissue Res*.
1157 355:267-278.

1158 Luscher, T.F., and M. Barton. 2000. Endothelins and endothelin receptor antagonists: therapeutic
1159 considerations for a novel class of cardiovascular drugs. *Circulation*. 102:2434-2440.

1160 Madisen, L., T.A. Zwingman, S.M. Sunkin, S.W. Oh, H.A. Zariwala, H. Gu, L.L. Ng, R.D. Palmiter,
1161 M.J. Hawrylycz, A.R. Jones, E.S. Lein, and H. Zeng. 2010. A robust and high-throughput
1162 Cre reporting and characterization system for the whole mouse brain. *Nature*
1163 *neuroscience*. 13:133-140.

1164 Mahar, M., and V. Cavalli. 2018. Intrinsic mechanisms of neuronal axon regeneration. *Nat Rev*
1165 *Neurosci*. 19:323-337.

1166 Maita, K.C., J.P. Garcia, F.R. Avila, R.A. Torres-Guzman, O. Ho, C.C.S. Chini, E.N. Chini, and
1167 A.J. Forte. 2023. Evaluation of the Aging Effect on Peripheral Nerve Regeneration: A
1168 Systematic Review. *J Surg Res*. 288:329-340.

1169 Maniglier, M., M. Vidal, C. Bachelin, C. Deboux, J. Chazot, B. Garcia-Diaz, and A. Baron-Van
1170 Evercooren. 2022. Satellite glia of the adult dorsal root ganglia harbor stem cells that yield

1171 glia under physiological conditions and neurons in response to injury. *Stem Cell Reports*.
1172 17:2467-2483.

1173 Mapps, A.A., M.B. Thomsen, E. Boehm, H. Zhao, S. Hattar, and R. Kuruvilla. 2022. Diversity of
1174 satellite glia in sympathetic and sensory ganglia. *Cell reports*. 38:110328.

1175 Maruoka, H., K. Kubota, R. Kurokawa, S. Tsuruno, and T. Hosoya. 2011. Periodic organization
1176 of a major subtype of pyramidal neurons in neocortical layer V. *The Journal of*
1177 *neuroscience : the official journal of the Society for Neuroscience*. 31:18522-18542.

1178 Mazaud, D., A. Capano, and N. Rouach. 2021. The many ways astroglial connexins regulate
1179 neurotransmission and behavior. *Glia*. 69:2527-2545.

1180 Nagashima, K., and K. Oota. 1974. A histopathological study of the human spinal ganglia. 1.
1181 Normal variations in aging. *Acta Pathol Jpn*. 24:333-344.

1182 Newman, J.H., S. Kar, and P. Kirkpatrick. 2007. Ambrisentan. *Nat Rev Drug Discov*. 6:697-698.

1183 Oblinger, M.M., and R.J. Lasek. 1984. A conditioning lesion of the peripheral axons of dorsal root
1184 ganglion cells accelerates regeneration of only their peripheral axons. *The Journal of*
1185 *neuroscience : the official journal of the Society for Neuroscience*. 4:1736-1744.

1186 Ohara, P.T., J.P. Vit, A. Bhargava, and L. Jasmin. 2008. Evidence for a role of connexin 43 in
1187 trigeminal pain using RNA interference in vivo. *J Neurophysiol*. 100:3064-3073.

1188 Painter, M.W., A. Brosius Lutz, Y.C. Cheng, A. Latremoliere, K. Duong, C.M. Miller, S. Posada,
1189 E.J. Cobos, A.X. Zhang, A.J. Wagers, L.A. Havton, B. Barres, T. Omura, and C.J. Woolf.
1190 2014. Diminished Schwann cell repair responses underlie age-associated impaired axonal
1191 regeneration. *Neuron*. 83:331-343.

1192 Pannese, E. 1981. The satellite cells of the sensory ganglia. *Advances in anatomy, embryology,*
1193 *and cell biology*. 65:1-111.

1194 Pannese, E. 2010. The structure of the perineuronal sheath of satellite glial cells (SGCs) in
1195 sensory ganglia. *Neuron glia biology*. 6:3-10.

1196 Pannese, E., M. Ledda, C. Martinelli, and P. Sartori. 1997. Age-related decrease of the
1197 perineuronal satellite cell number in the rabbit spinal ganglia. *J Peripher Nerv Syst*. 2:77-
1198 81.

1199 Pannese, E., P. Procacci, M. Ledda, and V. Conte. 1996. Age-related reduction of the satellite
1200 cell sheath around spinal ganglion neurons in the rabbit. *J Neurocytol*. 25:137-146.

1201 Patel, P., C.N. Buchanan, M.D. Zdradzinski, P.K. Sahoo, A.N. Kar, S.J. Lee, L.S. Vaughn, A.
1202 Urisman, J. Oses-Prieto, M. Dell'Orco, D.E. Cassidy, I.D. Costa, S. Miller, E. Thames, T.P.
1203 Smith, A.L. Burlingame, N. Perrone-Bizzozero, and J.L. Twiss. 2022. Intra-axonal
1204 translation of Khsrp mRNA slows axon regeneration by destabilizing localized mRNAs.
1205 *Nucleic acids research*. 50:5772-5792.

1206 Peacock, A.J., W. Zamboni, and C.D. Vizza. 2015. Ambrisentan for the treatment of adults with
1207 pulmonary arterial hypertension: a review. *Curr Med Res Opin*. 31:1793-1807.

1208 Pestronk, A., D.B. Drachman, and J.W. Griffin. 1980. Effects of aging on nerve sprouting and
1209 regeneration. *Experimental neurology*. 70:65-82.

1210 Pinho-Ribeiro, F.A., S.M. Borghi, L. Staurengo-Ferrari, G.B. Filgueiras, C. Estanislau, and W.A.
1211 Verri, Jr. 2014. Bosentan, a mixed endothelin receptor antagonist, induces
1212 antidepressant-like activity in mice. *Neuroscience letters*. 560:57-61.

1213 Pomonis, J.D., S.D. Rogers, C.M. Peters, J.R. Ghilardi, and P.W. Mantyh. 2001. Expression and
1214 localization of endothelin receptors: implications for the involvement of peripheral glia in
1215 nociception. *The Journal of neuroscience : the official journal of the Society for*
1216 *Neuroscience*. 21:999-1006.

1217 Procacci, P., V. Magnaghi, and E. Pannese. 2008. Perineuronal satellite cells in mouse spinal
1218 ganglia express the gap junction protein connexin43 throughout life with decline in old age.
1219 *Brain research bulletin*. 75:562-569.

1220 Renthal, W., I. Tochitsky, L. Yang, Y.C. Cheng, E. Li, R. Kawaguchi, D.H. Geschwind, and C.J.
1221 Woolf. 2020. Transcriptional Reprogramming of Distinct Peripheral Sensory Neuron
1222 Subtypes after Axonal Injury. *Neuron*.

1223 Retamal, M.A., M.A. Riquelme, J. Stehberg, and J. Alcayaga. 2017. Connexin43 Hemichannels
1224 in Satellite Glial Cells, Can They Influence Sensory Neuron Activity? *Front Mol Neurosci*.
1225 10:374.

1226 Rishal, I., and M. Fainzilber. 2014. Axon-soma communication in neuronal injury. *Nat Rev*
1227 *Neurosci*. 15:32-42.

1228 Robertson, R.T., S.T. Levine, S.M. Haynes, P. Gutierrez, J.L. Baratta, Z. Tan, and K.J. Longmuir.
1229 2015. Use of labeled tomato lectin for imaging vasculature structures. *Histochem Cell Biol*.
1230 143:225-234.

1231 Rozyczka, J., M. Figiel, and J. Engele. 2005. Chronic endothelin exposure inhibits connexin43
1232 expression in cultured cortical astroglia. *J Neurosci Res*. 79:303-309.

1233 Rubin, L.J., D.B. Badesch, R.J. Barst, N. Galie, C.M. Black, A. Keogh, T. Pulido, A. Frost, S. Roux,
1234 I. Leconte, M. Landzberg, and G. Simonneau. 2002. Bosentan therapy for pulmonary
1235 arterial hypertension. *N Engl J Med*. 346:896-903.

1236 Sahoo, P.K., D.S. Smith, N. Perrone-Bizzozero, and J.L. Twiss. 2018. Axonal mRNA transport
1237 and translation at a glance. *J Cell Sci*. 131.

1238 Santos, A.L., and A.B. Lindner. 2017. Protein Posttranslational Modifications: Roles in Aging and
1239 Age-Related Disease. *Oxid Med Cell Longev*. 2017:5716409.

1240 Schmalbruch, H. 1987. The number of neurons in dorsal root ganglia L4-L6 of the rat. *Anat Rec*.
1241 219:315-322.

1242 Shin, J.E., Y. Cho, B. Beirowski, J. Milbrandt, V. Cavalli, and A. DiAntonio. 2012. Dual leucine
1243 zipper kinase is required for retrograde injury signaling and axonal regeneration. *Neuron*.
1244 74:1015-1022.

1245 Shin, J.E., S. Geisler, and A. DiAntonio. 2014. Dynamic regulation of SCG10 in regenerating
1246 axons after injury. *Experimental neurology*. 252:1-11.

1247 Skariah, G., and P.K. Todd. 2021. Translational control in aging and neurodegeneration. *Wiley*
1248 *Interdiscip Rev RNA*. 12:e1628.

1249 Smith, D.S., and J.H. Skene. 1997. A transcription-dependent switch controls competence of adult
1250 neurons for distinct modes of axon growth. *The Journal of neuroscience : the official*
1251 *journal of the Society for Neuroscience*. 17:646-658.

1252 Stauffer, B.L., C.M. Westby, and C.A. DeSouza. 2008. Endothelin-1, aging and hypertension.
1253 *Curr Opin Cardiol*. 23:350-355.

1254 Sutherland, T.C., A. Sefiani, D. Horvat, T.E. Huntington, Y. Lei, A.P. West, and C.G. Geoffroy.
1255 2021. Age-Dependent Decline in Neuron Growth Potential and Mitochondria Functions in
1256 Cortical Neurons. *Cells*. 10.

1257 Takasaki, C., R. Okada, A. Mitani, M. Fukaya, M. Yamasaki, Y. Fujihara, T. Shirakawa, K. Tanaka,
1258 and M. Watanabe. 2008. Glutamate transporters regulate lesion-induced plasticity in the
1259 developing somatosensory cortex. *The Journal of neuroscience : the official journal of the*
1260 *Society for Neuroscience*. 28:4995-5006.

1261 Tani, K., S. Maki-Yonekura, R. Kanno, T. Negami, T. Hamaguchi, M. Hall, A. Mizoguchi, B.M.
1262 Humbel, T. Terada, K. Yonekura, and T. Doi. 2024. Structure of endothelin ET(B) receptor-
1263 G(i) complex in a conformation stabilized by unique NPxxL motif. *Commun Biol*. 7:1303.

1264 Tasdemir-Yilmaz, O.E., N.R. Druckenbrod, O.O. Olukoya, W. Dong, A.R. Yung, I. Bastille, M.F.
1265 Pazyra-Murphy, A.A. Sitko, E.B. Hale, S. Vigneau, A.A. Gimelbrant, P.V. Kharchenko, L.V.
1266 Goodrich, and R.A. Segal. 2021. Diversity of developing peripheral glia revealed by single-
1267 cell RNA sequencing. *Dev Cell*. 56:2516-2535 e2518.

1268 Tedeschi, A., and F. Bradke. 2017. Spatial and temporal arrangement of neuronal intrinsic and
1269 extrinsic mechanisms controlling axon regeneration. *Current opinion in neurobiology*.
1270 42:118-127.

1271 Usoskin, D., A. Furlan, S. Islam, H. Abdo, P. Lonnerberg, D. Lou, J. Hjerling-Leffler, J.
1272 Haeggstrom, O. Kharchenko, P.V. Kharchenko, S. Linnarsson, and P. Ernfors. 2015.
1273 Unbiased classification of sensory neuron types by large-scale single-cell RNA
1274 sequencing. *Nature neuroscience*. 18:145-153.

1275 Valtcheva, M.V., B.A. Copits, S. Davidson, T.D. Sheahan, M.Y. Pullen, J.G. McCall, K. Dikranian,
1276 and R.W.t. Gereau. 2016. Surgical extraction of human dorsal root ganglia from organ
1277 donors and preparation of primary sensory neuron cultures. *Nature protocols*. 11:1877-
1278 1888.

1279 Vaughan, D.W. 1992. Effects of advancing age on peripheral nerve regeneration. *The Journal of*
1280 *comparative neurology*. 323:219-237.

1281 Verdu, E., D. Ceballos, J.J. Vilches, and X. Navarro. 2000. Influence of aging on peripheral nerve
1282 function and regeneration. *J Peripher Nerv Syst*. 5:191-208.

1283 Wujek, J.R., and R.J. Lasek. 1983. Correlation of axonal regeneration and slow component B in
1284 two branches of a single axon. *The Journal of neuroscience : the official journal of the*
1285 *Society for Neuroscience*. 3:243-251.

1286 Yanagisawa, M., H. Kurihara, S. Kimura, Y. Tomobe, M. Kobayashi, Y. Mitsui, Y. Yazaki, K. Goto,
1287 and T. Masaki. 1988. A novel potent vasoconstrictor peptide produced by vascular
1288 endothelial cells. *Nature*. 332:411-415.

1289 Yang, L., F. Dong, Q. Yang, P.F. Yang, R. Wu, Q.F. Wu, D. Wu, C.L. Li, Y.Q. Zhong, Y.J. Lu, X.
1290 Cheng, F.Q. Xu, L. Chen, L. Bao, and X. Zhang. 2017. FGF13 Selectively Regulates Heat
1291 Nociception by Interacting with Na(v)1.7. *Neuron*. 93:806-821 e809.

1292 Ydens, E., L. Amann, B. Asselbergh, C.L. Scott, L. Martens, D. Sichien, O. Mossad, T. Blank, S.
1293 De Prijck, D. Low, T. Masuda, Y. Saeys, V. Timmerman, R. Stumm, F. Ginhoux, M. Prinz,
1294 S. Janssens, and M. Guilliams. 2020. Profiling peripheral nerve macrophages reveals two
1295 macrophage subsets with distinct localization, transcriptome and response to injury.
1296 *Nature neuroscience*. 23:676-689.

1297 Yun, M.H. 2015. Changes in Regenerative Capacity through Lifespan. *Int J Mol Sci*. 16:25392-
1298 25432.

1299 Zhao, X.F., L.D. Huffman, H. Hafner, M. Athaiya, M.C. Finneran, A.L. Kalinski, R. Kohen, C. Flynn,
1300 R. Passino, C.N. Johnson, D. Kohrman, R. Kawaguchi, L.J.S. Yang, J.L. Twiss, D.H.
1301 Geschwind, G. Corfas, and R.J. Giger. 2022. The injured sciatic nerve atlas (iSNAT),
1302 insights into the cellular and molecular basis of neural tissue degeneration and
1303 regeneration. *Elife*. 11.

1304 Zhou, L., G. Kong, I. Palmisano, M.T. Cencioni, M. Danzi, F. De Virgiliis, J.S. Chadwick, G.
1305 Crawford, Z. Yu, F. De Winter, V. Lemmon, J. Bixby, R. Puttagunta, J. Verhaagen, C.
1306 Pospori, C. Lo Celso, J. Strid, M. Botto, and S. Di Giovanni. 2022. Reversible CD8 T cell-
1307 neuron cross-talk causes aging-dependent neuronal regenerative decline. *Science*.
1308 376:eabd5926.

1309 Zigmond, R.E., and F.D. Echevarria. 2019. Macrophage biology in the peripheral nervous system
1310 after injury. *Prog Neurobiol*. 173:102-121.

1311

Fig. 1

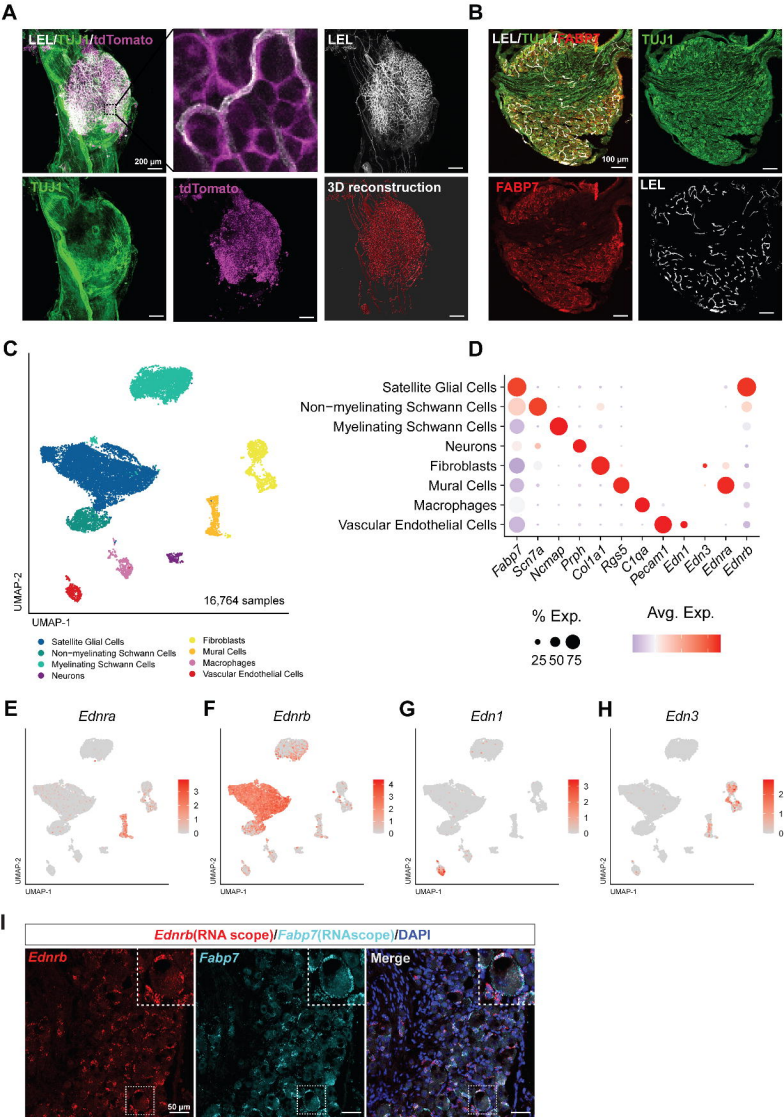
A
LEL/TUJ1/tdTomato
200 μm
LEL
TUJ1
tdTomato
3D reconstruction
B
LEL/TUJ1/FABP7
100 μm
TUJ1
FABP7
LEL
C
UMAP-2
UMAP-1
16,764 samples
Satellite Glial Cells
Non−myelinating Schwann Cells
Myelinating Schwann Cells
Neurons
Fibroblasts
Mural Cells
Macrophages
Vascular Endothelial Cells
D
Satellite Glial Cells
Non−myelinating Schwann Cells
Myelinating Schwann Cells
Neurons
Fibroblasts
Mural Cells
Macrophages
Vascular Endothelial Cells
Fabp7
Scn7a
Nomap
Prph
Col1a1
Rgs5
C1qa
Pecam1
Edn1
Edn3
Ednra
Ednrb
% Exp.
25 50 75
Avg. Exp.
E
Ednra
F
Ednrb
G
Edn1
H
Edn3
I
Ednrb(RNA scope)/Fabp7(RNAscope)/DAPI
Ednrb
Fabp7
Merge
50 μm

Fig. 2

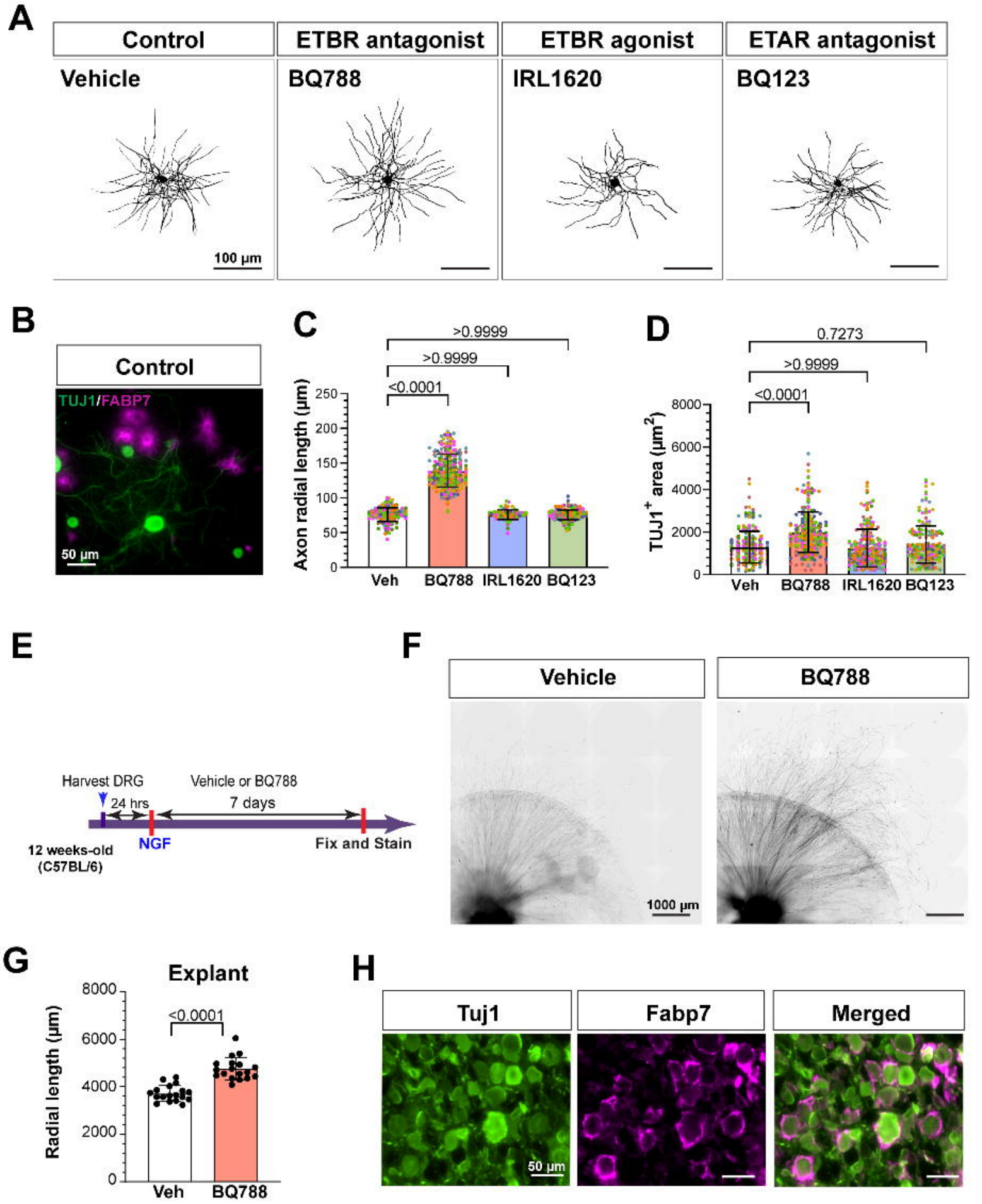
A
Control
ETBR antagonist
ETBR agonist
ETAR antagonist
Vehicle
BQ788
IRL1620
BQ123
100 µm
B
Control
TUJ1/FABP7
50 µm
C
>0.9999
>0.9999
<0.0001
Axon radial length (µm)
250
200
150
100
50
0
Veh
BQ788
IRL1620
BQ123
D
0.7273
>0.9999
<0.0001
TUJ1+ area (µm2)
8000
6000
4000
2000
0
Veh
BQ788
IRL1620
BQ123
E
Harvest DRG
24 hrs
Vehicle or BQ788
7 days
12 weeks-old
(C57BL/6)
NGF
Fix and Stain
F
Vehicle
BQ788
1000 µm
G
Explant
<0.0001
Radial length (µm)
8000
6000
4000
2000
0
Veh
BQ788
H
Tuj1
Fabp7
Merged
50 µm

Fig. 3

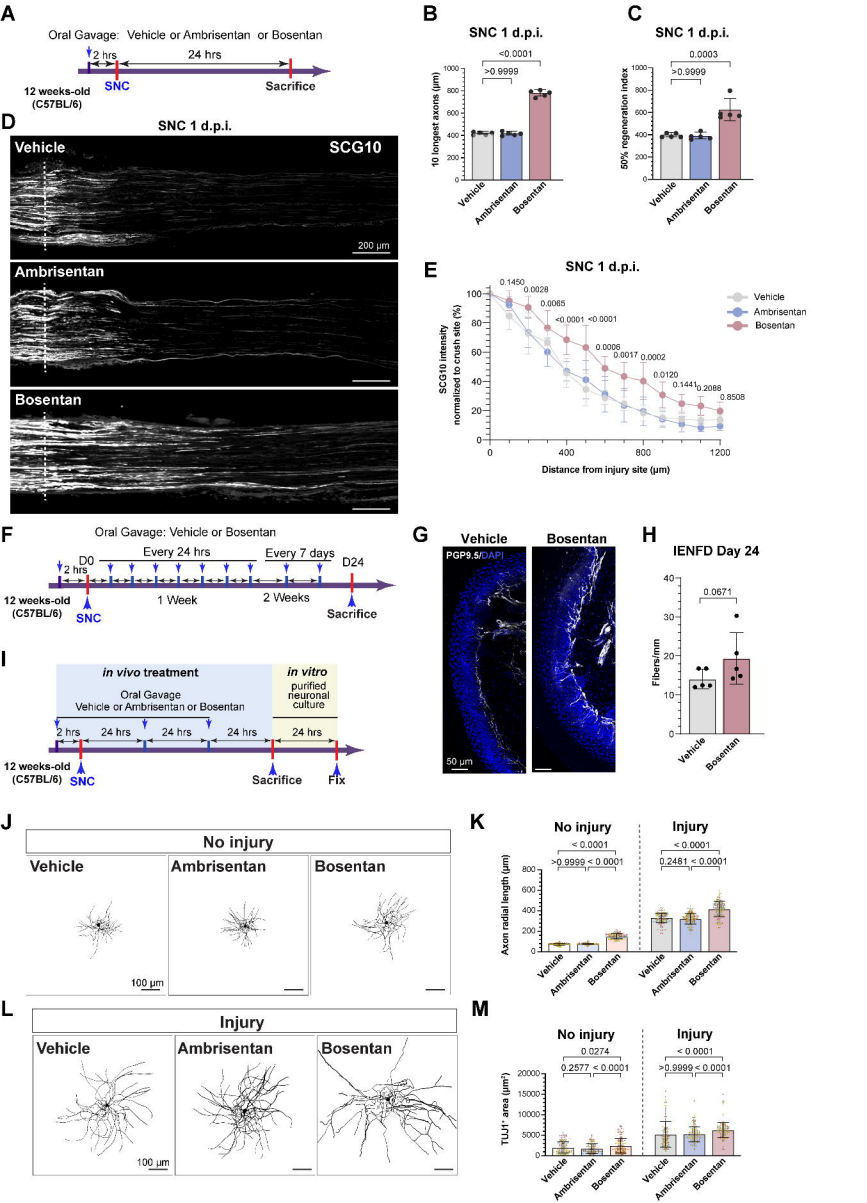
A
Oral Gavage: Vehicle or Ambrisentan or Bosentan
2 hrs
24 hrs
12 weeks-old (C57BL/6)
SNC
Sacrifice
B
SNC 1 d.p.i.
10 longest axons (µm)
<0.0001
>0.9999
Vehicle
Ambrisentan
Bosentan
C
SNC 1 d.p.i.
50% regeneration index
0.0003
>0.9999
D
SNC 1 d.p.i.
Vehicle
SCG10
200 µm
Ambrisentan
Bosentan
E
SNC 1 d.p.i.
SCG10 intensity normalized to crush site (%)
Distance from injury site (µm)
0.1450
0.0028
0.0085
<0.0001
<0.0001
0.0006
0.0017
0.0002
0.0120
0.1441
0.2088
0.8508
F
Oral Gavage: Vehicle or Bosentan
Every 24 hrs
Every 7 days
D0
D24
2 hrs
1 Week
2 Weeks
12 weeks-old (C57BL/6)
SNC
Sacrifice
G
Vehicle
Bosentan
PGP9.5/DAPI
50 µm
H
IENFD Day 24
Fibers/mm
0.0671
I
in vivo treatment
Oral Gavage
Vehicle or Ambrisentan or Bosentan
in vitro
purified neuronal culture
2 hrs
24 hrs
12 weeks-old (C57BL/6)
SNC
Sacrifice
Fix
J
No injury
Vehicle
Ambrisentan
Bosentan
100 µm
K
No injury
Injury
Axon radial length (µm)
< 0.0001
>0.9999
< 0.0001
0.2481
L
Injury
Vehicle
Ambrisentan
Bosentan
100 µm
M
No injury
Injury
TUJ1+ area (µm²)
0.0274
0.2577
< 0.0001
>0.9999

Fig. 4

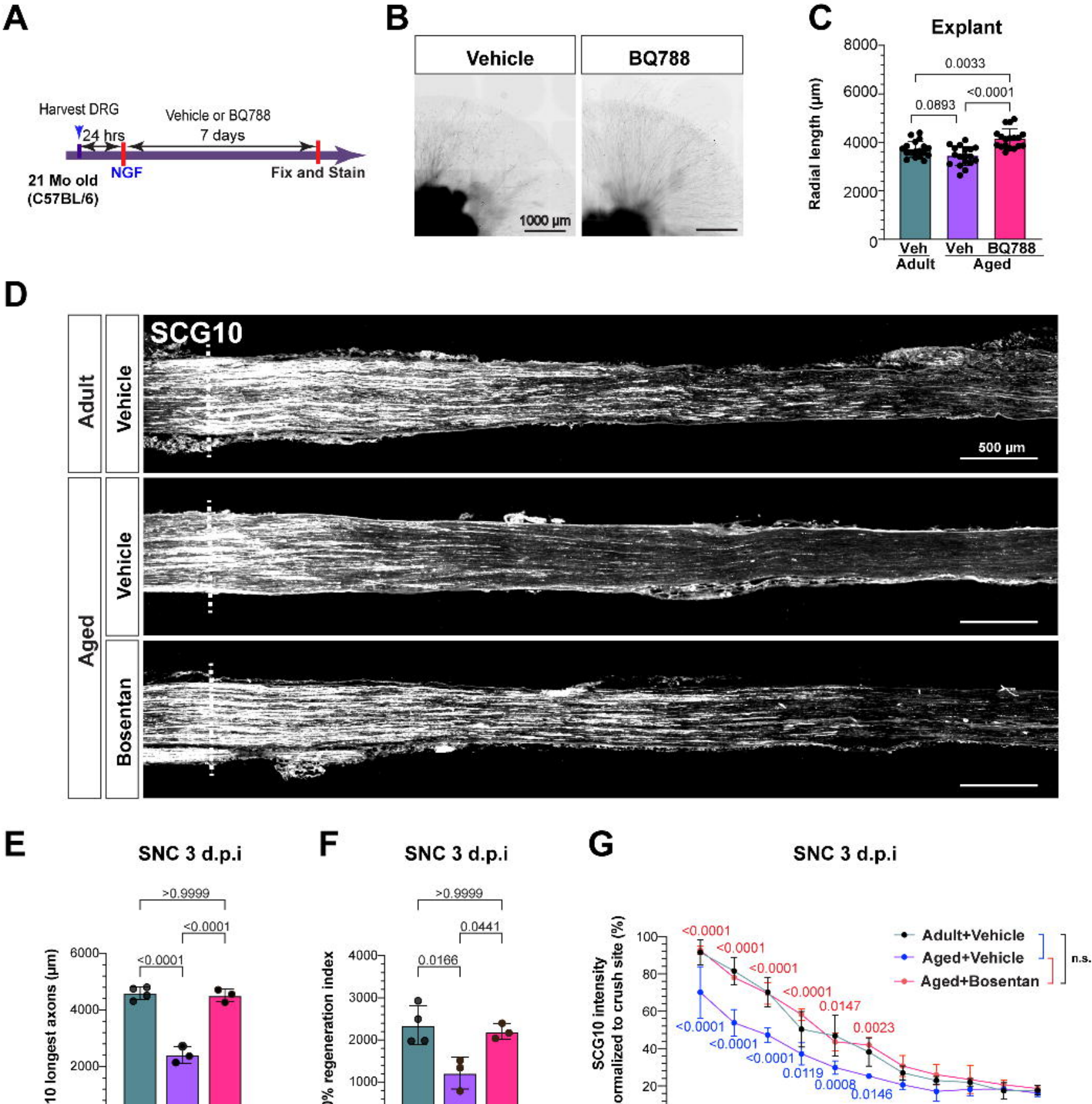
A
Harvest DRG
24 hrs
Vehicle or BQ788
7 days
NGF
Fix and Stain
21 Mo old
(C57BL/6)
B
Vehicle
BQ788
1000 µm
C
Explant
Radial length (µm)
0.0033
0.0893
<0.0001
Veh
Veh
BQ788
Adult
Aged
D
SCG10
Adult
Vehicle
Aged
Vehicle
Bosentan
500 µm
E
SNC 3 d.p.i
10 longest axons (µm)
>0.9999
<0.0001
<0.0001
Veh
Veh
Bosentan
Adult
Aged
F
SNC 3 d.p.i
50% regeneration index
>0.9999
0.0441
0.0166
Veh
Veh
Bosentan
Adult
Aged
G
SNC 3 d.p.i
SCG10 intensity normalized to crush site (%)
Distance from injury site (µm)
Adult+Vehicle
Aged+Vehicle
Aged+Bosentan
n.s.
<0.0001
<0.0001
<0.0001
<0.0001
0.0147
0.0023
<0.0001
<0.0001
<0.0001
0.0119
0.0008
0.0146

Fig.5

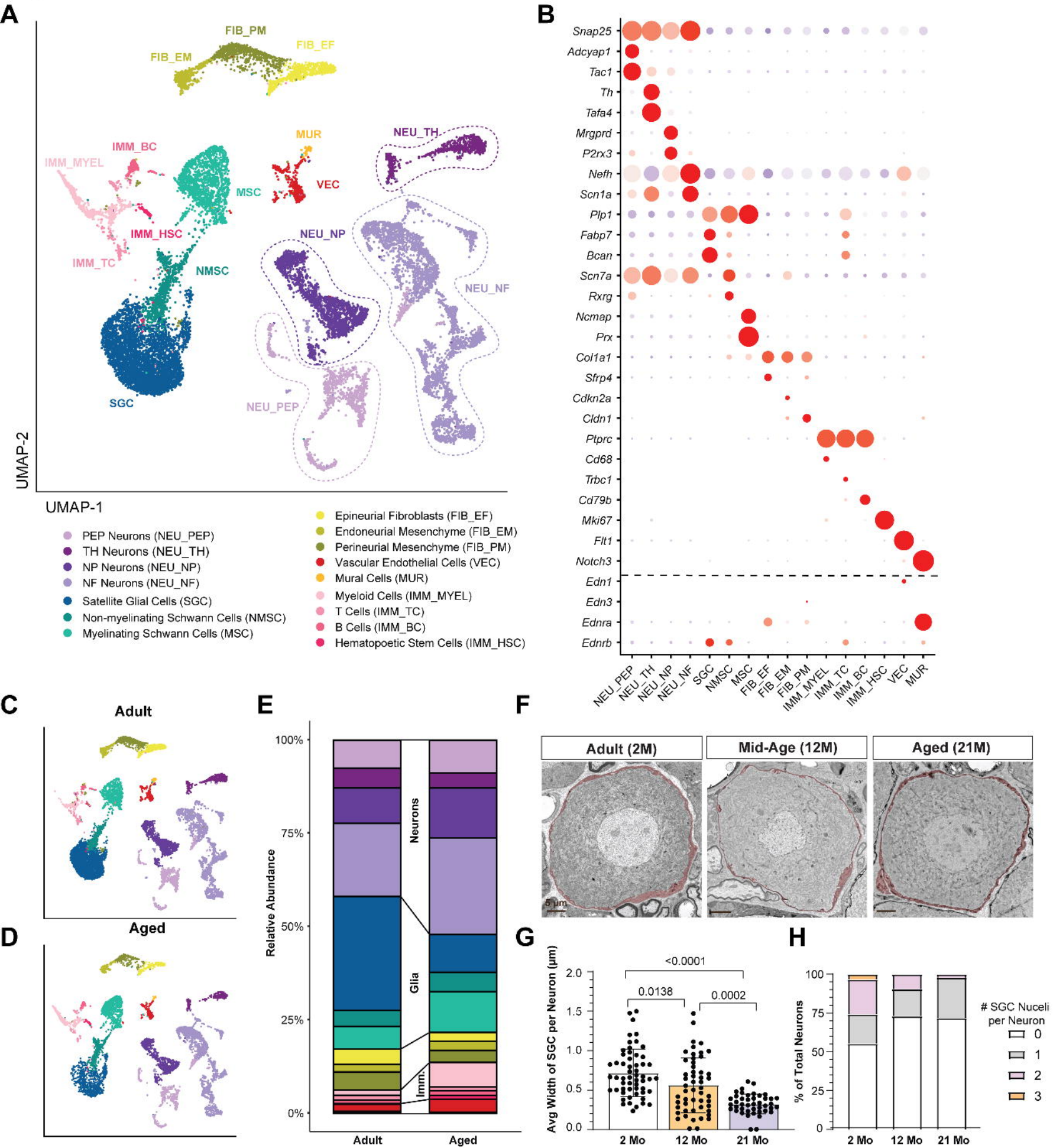
A
FIB_PM
FIB_EM
FIB_EF
MUR
NEU_TH
IMM_BC
IMM_MYEL
MSC
VEC
IMM_HSC
NEU_NP
IMM_TC
NMSC
NEU_NF
SGC
NEU_PEP
UMAP-2
UMAP-1
PEP Neurons (NEU_PEP)
TH Neurons (NEU_TH)
NP Neurons (NEU_NP)
NF Neurons (NEU_NF)
Satellite Glial Cells (SGC)
Non-myelinating Schwann Cells (NMSC)
Myelinating Schwann Cells (MSC)
Epineurial Fibroblasts (FIB_EF)
Endoneurial Mesenchyme (FIB_EM)
Perineurial Mesenchyme (FIB_PM)
Vascular Endothelial Cells (VEC)
Mural Cells (MUR)
Myeloid Cells (IMM_MYEL)
T Cells (IMM_TC)
B Cells (IMM_BC)
Hematopoetic Stem Cells (IMM_HSC)
B
Snap25
Adcyap1
Tac1
Th
Tafa4
Mrgprd
P2rx3
Nefh
Scn1a
Plp1
Fabp7
Bcan
Scn7a
Rxrg
Ncmap
Prx
Col1a1
Sfrp4
Cdkn2a
Cldn1
Ptprc
Cd68
Trbc1
Cd79b
Mki67
Flt1
Notch3
Edn1
Edn3
Ednra
Ednrb
NEU_PEP
NEU_TH
NEU_NP
NEU_NF
SGC
NMSC
MSC
FIB_EF
FIB_EM
FIB_PM
IMM_MYEL
IMM_TC
IMM_BC
IMM_HSC
VEC
MUR
C
Adult
D
Aged
E
Relative Abundance
100%
75%
50%
25%
0%
Neurons
Glia
Imm.
Adult
Aged
F
Adult (2M)
Mid-Age (12M)
Aged (21M)
5 µm
G
Avg Width of SGC per Neuron (µm)
2.0
1.5
1.0
0.5
0.0
<0.0001
0.0138
0.0002
2 Mo
12 Mo
21 Mo
H
% of Total Neurons
100
75
50
25
0
2 Mo
12 Mo
21 Mo
SGC Nuceli per Neuron
0
1
2
3

Fig. 6

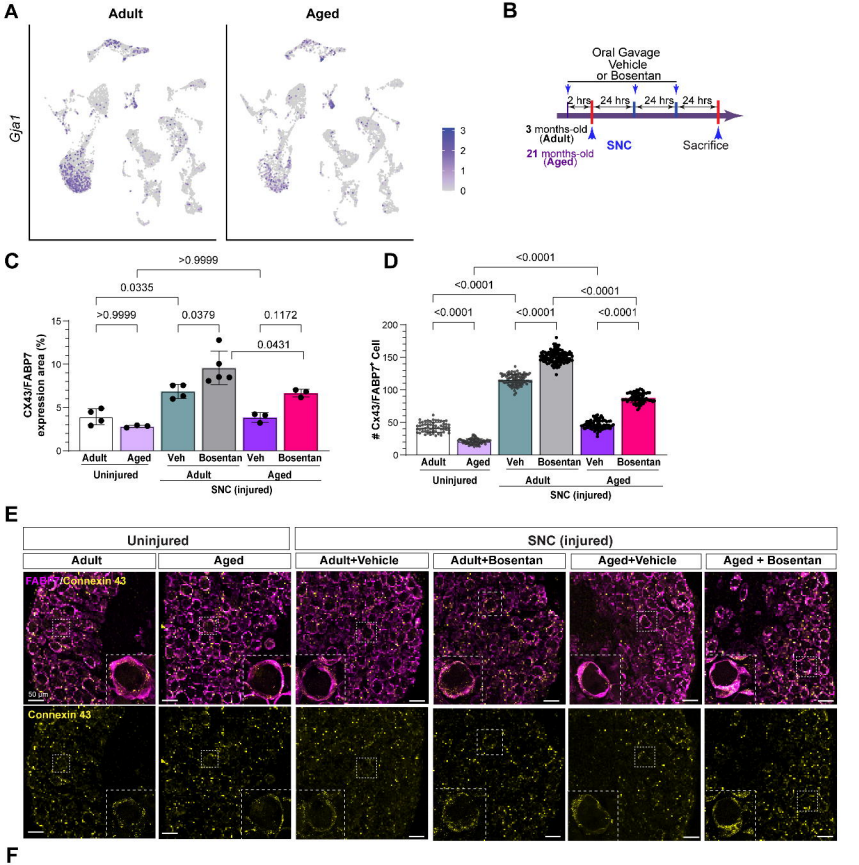
A
Adult
Aged
Gja1
3
2
1
0
B
Oral Gavage
Vehicle
or Bosentan
2 hrs
24 hrs
24 hrs
24 hrs
3 months-old
(Adult)
21 months-old
(Aged)
SNC
Sacrifice
C
>0.9999
0.0335
>0.9999
0.0379
0.1172
0.0431
CX43/FABP7
expression area (%)
Adult
Aged
Veh
Bosentan
Veh
Bosentan
Uninjured
Adult
Aged
SNC (injured)
D
<0.0001
<0.0001
<0.0001
<0.0001
<0.0001
<0.0001
Cx43/FABP7+ Cell
Adult
Aged
Veh
Bosentan
Veh
Bosentan
Uninjured
Adult
Aged
SNC (injured)
E
Uninjured
SNC (injured)
Adult
Aged
Adult+Vehicle
Adult+Bosentan
Aged+Vehicle
Aged + Bosentan
FABP7/Connexin 43
50 µm
Connexin 43
F
Adult
Cx43
ET-1
ETBR
Bosentan
Axon
Regeneration
Nerve Injury
Aged
Cx43
ET-1
ETBR
Bosentan
Axon
Regeneration
Nerve Injury

Figure 1- Figure Supplement 1

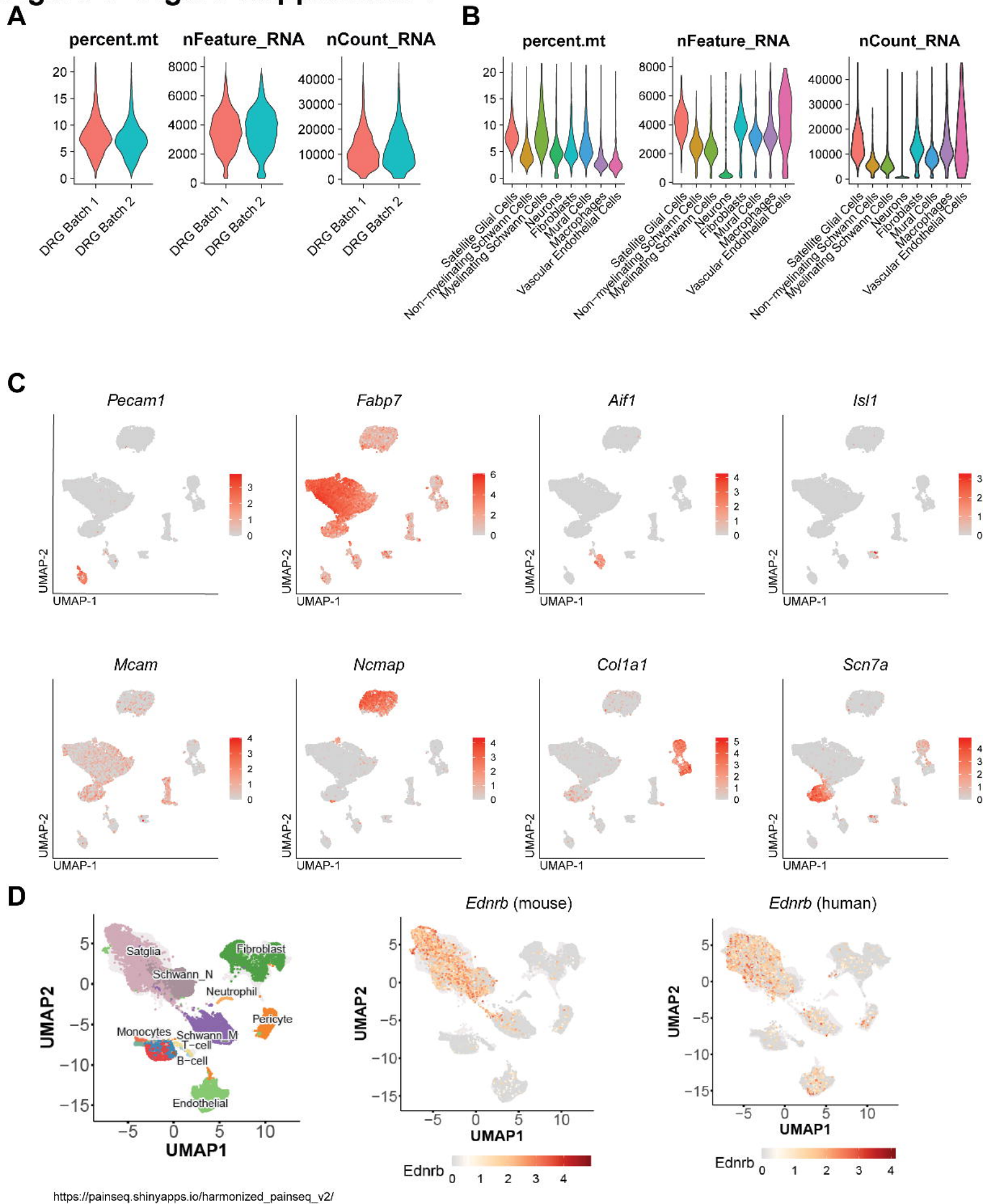

Figure 3- Figure Supplement 1

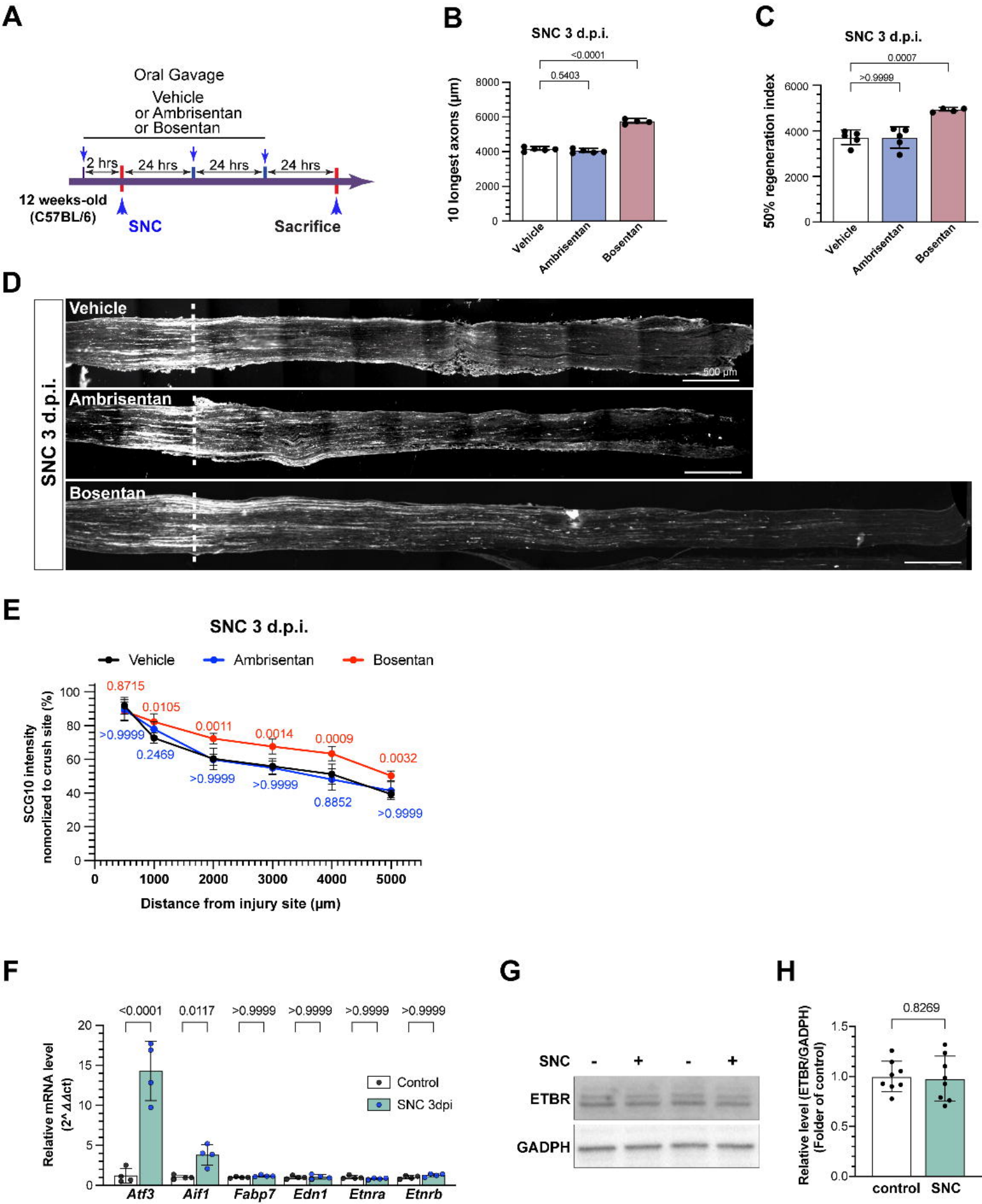

Figure 3- Figure Supplement 2

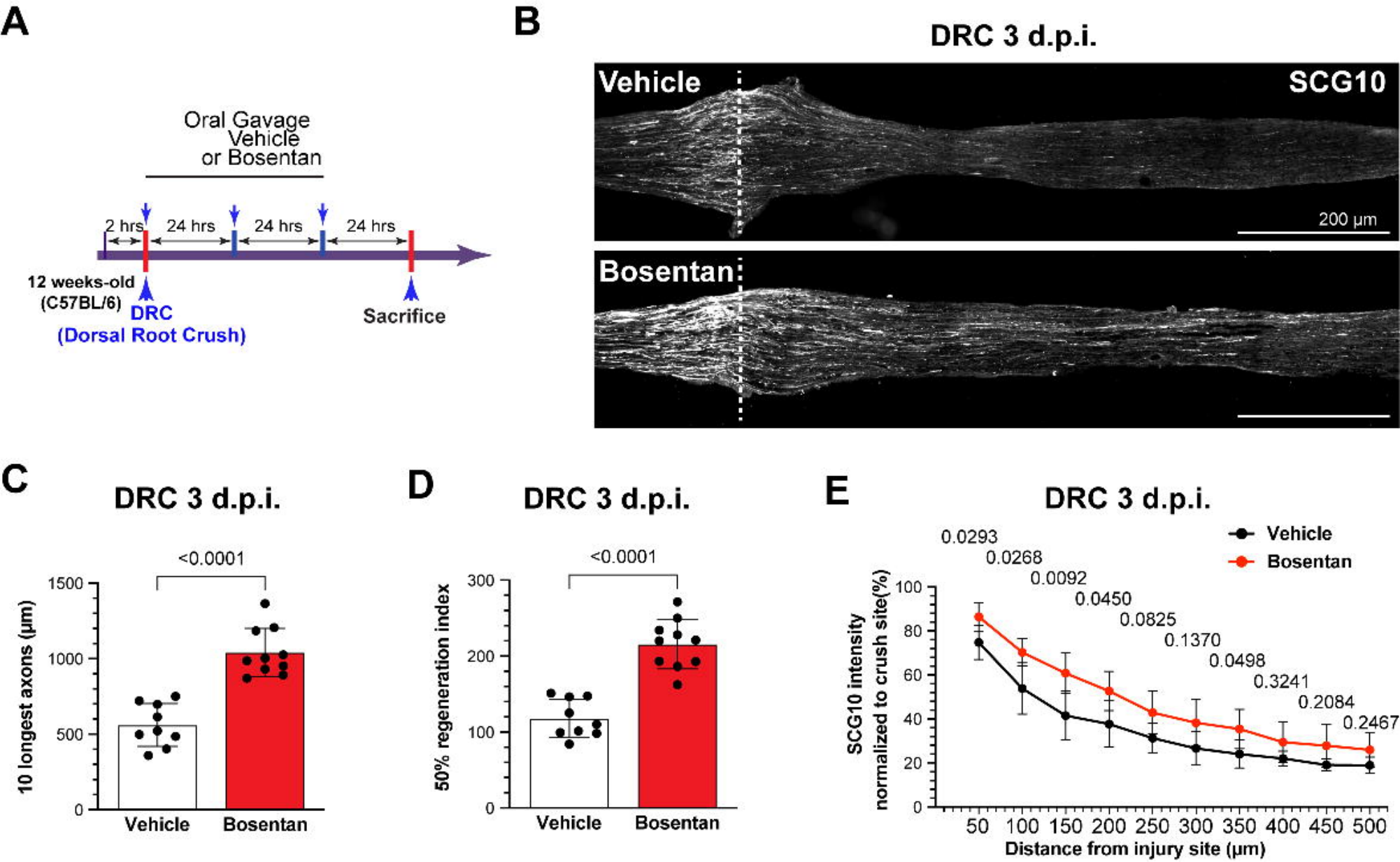

Figure 4- Figure Supplement 1

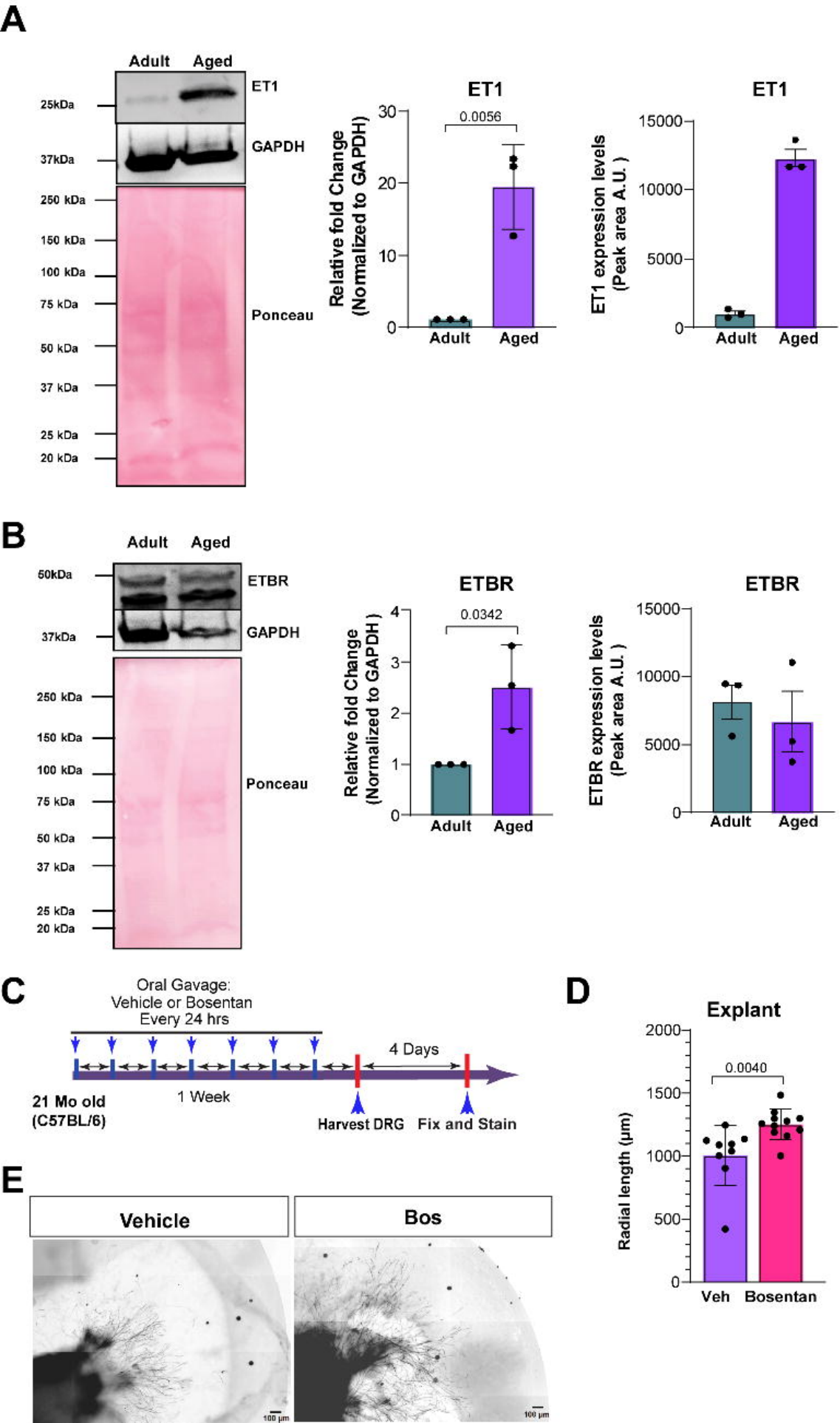

Figure 5- Figure Supplement 1

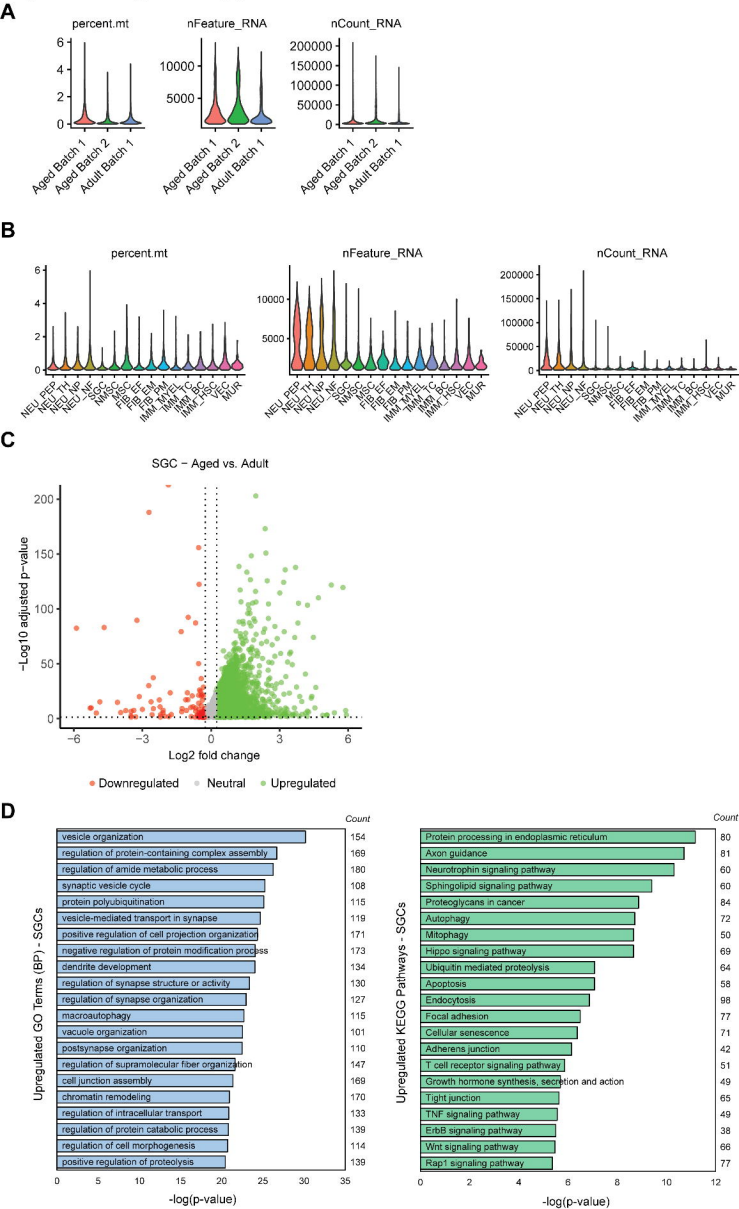
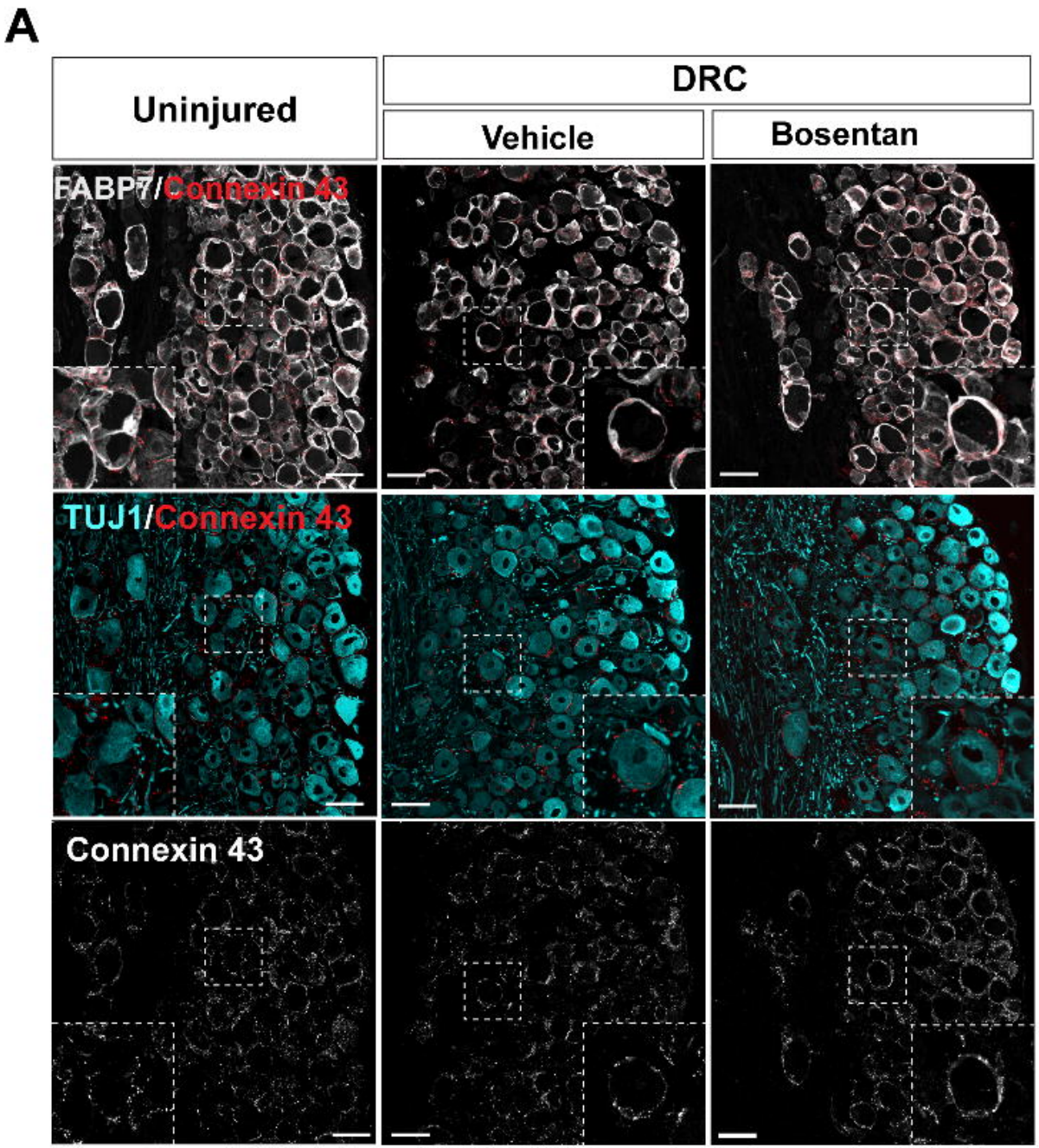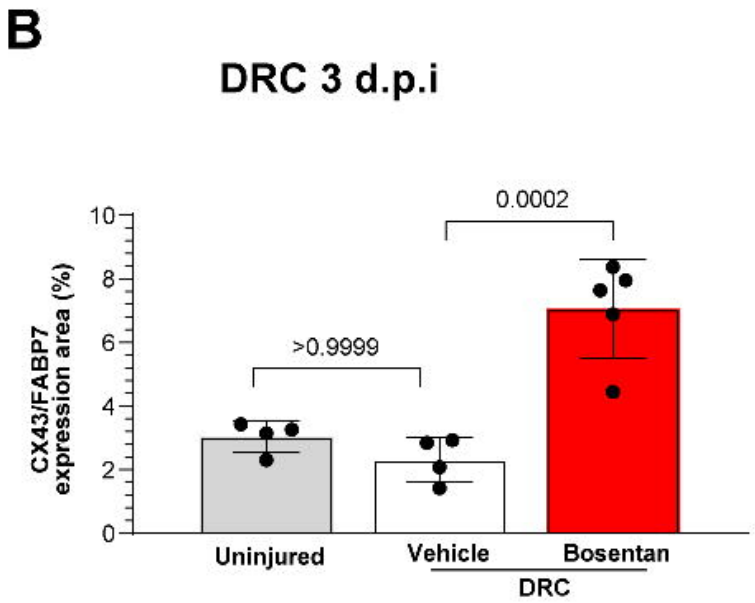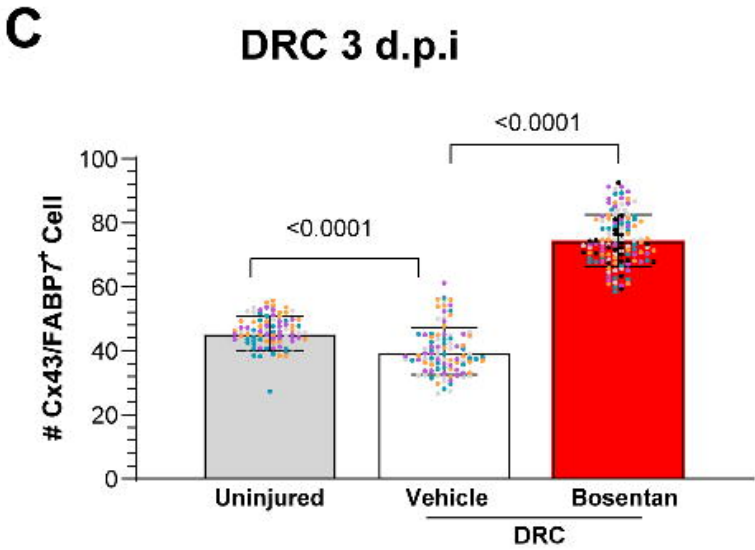
Figure 6- Figure Supplement 1